Supplementary Information: Programmable morphing of topological modes in non-Hermitian elastic continua: continuum characterization and physical realization

Honghua Qian,[1,*] Jiaji Chen,[1,*] Qian Wu,[2,*] Nan Shao,[1] Shaoyun Wang,[1,†] and Guoliang Huang[2,‡]

[1] *Department of Mechanical and Aerospace Engineering, University of Missouri, Columbia, MO 65211, USA*

[2] *Department of Mechanics and Engineering Science, College of Engineering, Peking University, Beijing 100871, PR China*

(Dated: June 13, 2026)

CONTENTS

1. Geometric and electrical parameters for the non-Hermitian topological metabeam and stacked metaplate 2

2. Piezoelectricity-based sensing and actuating 2

3. Boundary value problems of non-Hermitian topological beam 4

4. Two-band reduction and effective Dirac boundary-value problem 5
   A. Nearly-free-electron reduction and effective Dirac Hamiltonian. 5
   B. Effective boundary conditions under free ends. 7
   C. Remarks on the effective Dirac boundary-value problem. 8

5. Unitary transformation and connection to the non-Hermitian Rice–Mele Dirac form 8

6. Dispersion relation and topological Chern number in non-Hermitian system 9

7. Asymptotic analysis of the Dirac boundary-value problem and the generalized Brillouin zone 9

8. Non-Hermitian topological edge modes 10
   A. Eigenvalues of topological edge modes 10
   B. Localization rate of topological edge modes 11

9. Non-Hermitian morphing of topological modes 11
   A. Critical delocalization condition for the topological edge mode 12
   B. Spectral winding transition referenced to the TEM frequency 12

10. Boundary truncation for unidirectional localized TEM 12

11. Transfer matrix method for wave dispersion with PBC and eigenfrequency with OBC 12

12. Robustness of non-Hermitian morphing of topological edge modes 15

13. Experimental setup 16

14. Design principle of 2D stack metaplate 16

15. Non-Hermitian phase transition and frequency spectrum in 2D metaplate 18

16. More defects on splitting pattern of robust topological mode in metaplate 21

References 24

* These two authors contributed equally.

† Corresponding author: shaoyunwang@missouri.edu

‡ Corresponding author: guohuang@pku.edu.cn

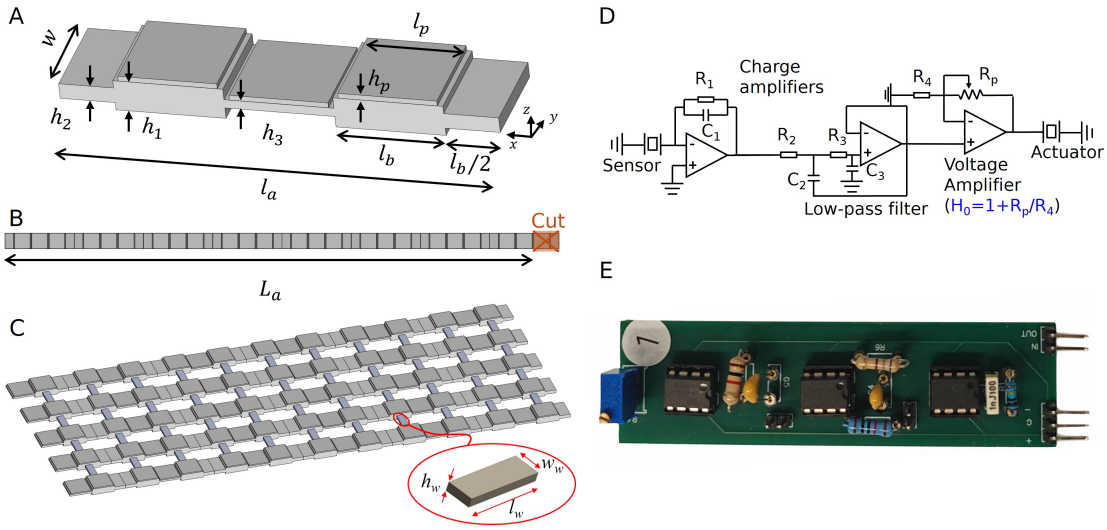

FIG. S1. Geometric and electrical parameters of the metabeam and metaplate. (A) Geometric parameters of the unit cell. (B) Beam configuration with boundary termination (cut) used to suppress the opposite-edge hybrid mode. (C) Stacked metaplate assembled from multiple metabeams. (D) External circuit architecture used to implement the active non-Hermitian feedback. (E) Photograph of the realized circuit.

1. GEOMETRIC AND ELECTRICAL PARAMETERS FOR THE NON-HERMITIAN TOPOLOGICAL METABEAM AND STACKED METAPLATE

Figure S1 summarizes the geometric layout and the external circuit architecture used in the experiments. The unit cell geometry (Fig. S1A), the finite metabeam with boundary termination (Fig. S1B), and the stacked metaplate configuration (Fig. S1C) follow the designs described in the main text. All geometric dimensions, material properties, and circuit component values used for fabrication and modeling are provided in Table S1. The mechanical substrates are made of stainless steel and machined by milling. Piezoelectric patches (PZT-5A) are bonded to the substrate using conductive epoxy (CircuitWorks CW2400). For both the metabeam and metaplate specimens, only the sensor–actuator pair is retained in the final unit cell to realize a single-direction TEM.

The nonlocal and nonreciprocal coupling is implemented by an external analog feedback circuit, as shown in Fig. S1D,E. In this circuit, the sensor piezoelectric patch provides a charge output that is first converted to a voltage by a charge amplifier (R_1, C_1), then conditioned by an active low-pass filter (R_2, R_3, C_2, C_3) to suppress high-frequency noise and stabilize the feedback, and finally boosted by a voltage amplifier stage with adjustable gain $H_0 = 1 + R_p/R_4$ to drive the actuator patch. This cascaded amplification–filtering–amplification architecture realizes the programmed nonlocal, nonreciprocal curvature feedback discussed in the main text. All circuit component values are listed in Table S1. The circuit boards are powered by a DC supply.

2. PIEZOELECTRICITY-BASED SENSING AND ACTUATING

This section derives the electromechanical mapping of the in-cell sensor-actuator pair and clarifies how the external circuit produces an active (and generally non-Hermitian) feedback moment. We consider the dominant z-x mode of the bonded piezoelectric patches: axial mechanical response along the beam axis (x-direction) coupled to an electric field through the patch thickness (z-direction). With the patch being thin and surface-bonded, the coupled problem is reduced to an in-plane description under a plane-stress approximation in the patch, while retaining the thickness-direction electric field $\mathcal{E}_z$.

The linear constitutive relations of the piezoelectric layer are written as [1]

$$\begin{aligned} \mathcal{S}_x &= S_{xx}^E \, \mathcal{T}_x + d_{zx} \, \mathcal{E}_z, \\ \mathcal{D}_z &= \epsilon_{zz}^T \, \mathcal{E}_z + d_{zx} \, \mathcal{T}_x, \end{aligned} \tag{S1}$$

where $\mathcal{S}_x$ and $\mathcal{T}_x$ denote the axial strain and axial stress in the piezoelectric patch, and $\mathcal{E}_z$ and $\mathcal{D}_z$ denote the electric field and electric displacement in the thickness direction. The coefficients S_{xx}^E, ϵ_{zz}^T, and d_{zx} are, respectively, the compliance at constant electric field, dielectric permittivity at constant stress, and piezoelectric coupling coefficient (often denoted d_{31}). For the PZT-5A patches used in our experiments we take $S_{xx}^E = 1.64\times10^{-11}\ \mathrm{Pa}^{-1}$, $\epsilon_{zz}^T = 1900$, and $d_{zx} = 1.71\times10^{-10}\ \mathrm{C/N}$.

For the sensor patch connected to a charge amplifier, the input node is maintained close to a virtual ground within the

TABLE S1. Parameters of geometry, material properties, and electrical circuit.

Geometric parameters			
Parameter	Value	Parameter	Value
h_1	3 mm	h_2	1.5 mm
h_3	0.85 mm	h_p	0.5 mm
l_p	9 mm	w	9 mm
l_b	10 mm	L_a	305 mm
l_w	9 mm	w_w	3 mm
h_w	1 mm	l_a	40 mm
Electrical parameters			
Parameter	Value	Parameter	Value
R_1	1 MΩ	R_2	1.5 kΩ
R_3	6.8 kΩ	R_4	1 kΩ
R_p	0–10 kΩ	C_1	1 nF
C_2	4.7 nF	C_3	0.47 nF
Material properties of the substrate beam (stainless steel)			
Parameter	Value	Parameter	Value
E_b	210 GPa	ρ_b	7800 kg/m^3
κ	11/12	G	90 GPa
Material properties of the piezoelectric patches (PZT-5A)			
Parameter	Value	Parameter	Value
S^{E}_{xx}	1.64×10^{-11} Pa^{-1}	$\varepsilon^{\mathrm{T}}_{zz}$	1900
d_{zx}	-1.71×10^{-10} C/N		

operating bandwidth, which is well approximated by a short-circuit electrical condition,

$$\mathcal{E}_z \approx 0. \tag{S2}$$

Under $\mathcal{E}_z \approx 0$, Eq. (S1) gives $\mathcal{T}_x = \mathcal{S}_x / S^E_{xx}$ and $\mathcal{D}_z = d_{zx}\mathcal{T}_x$. The output charge flowing into the charge amplifier equals the integral of $\mathcal{D}_z$ over the electrode area,

$$\mathcal{Q}_s = \int_{\text{electrode area}} \mathcal{D}_z \, dS \approx \mathcal{D}_z \, l_p w_p = \frac{d_{zx}}{S^E_{xx}} \mathcal{S}_x \, l_p w_p, \tag{S3}$$

where l_p and w_p are the patch length and width. The axial strain in the bonded patch is generated by beam bending. For small deflection of a slender beam, the axial strain at a distance z from the neutral axis is proportional to the curvature,

$$\mathcal{S}_x(x) = -z \, b(x), \qquad b(x) = \frac{\partial^2 w(x)}{\partial x^2}, \tag{S4}$$

where $w(x)$ is the transverse displacement and z is the offset between the effective sensing plane of the patch and the beam neutral axis (determined by the substrate thickness, patch thickness, and bonding layer). The charge amplifier converts $\mathcal{Q}_s$ to the measured sensor voltage V_s. For an ideal charge amplifier with feedback capacitance C_1 (listed in Table S1), one has

$$V_s = -\frac{\mathcal{Q}_s}{C_1}. \tag{S5}$$

Combining Eqs. (S3)–(S5) yields the curvature-to-voltage relation

$$V_s(x) = \frac{d_{zx} l_p w_p z}{S^E_{xx} C_1} \frac{\partial^2 w(x)}{\partial x^2}. \tag{S6}$$

For the actuator patch, the external circuit prescribes an actuation voltage proportional to the sensed voltage according to the circuit topology in Fig. S1D,

$$V_A = H_0 \, V_s, \tag{S7}$$

where H_0 is designed as a programmable real-valued gain. Although a low-pass filter is incorporated in the circuit (Fig. S1D), its cutoff frequency (33.5 kHz) is intentionally chosen to be much higher than the operating topological-mode frequency (approximately 1.5 kHz). Therefore, within the frequency range of interest the filter introduces negligible amplitude attenuation and phase lag, and we treat H_0 as frequency-independent and real-valued in the analytical modeling. The corresponding thickness-direction electric field is

$$\mathcal{E}_z = -\frac{V_A}{h_p} = -\frac{H_0}{h_p} V_s, \tag{S8}$$

with h_p the patch thickness. Through the converse piezoelectric effect, this electric field generates an equivalent bending moment on the beam. Following standard bonded-patch beam models [2, 3], the actuator-induced moment can be expressed in the compact feedback form

$$M(x) = -\alpha_c\, H_0\, \frac{\partial^2 w(x)}{\partial x^2}, \tag{S9}$$

where $\alpha_c = S_x(\epsilon_{zz}^{\mathrm{T}} w_p \delta x d_{zx} l_p w_p)/(d_{zx} S_{xx}^E C_1)$ denotes the coupling coefficient that collects the piezoelectric constants, patch geometry (l_p, w_p, h_p), the lever arm z, and the charge-amplifier calibration (through C_1), as well as the composite-section moment conversion associated with a surface-bonded patch [3]. Equation (S9) shows that the actuator behaves as a tunable, curvature-proportional moment source whose strength and phase are controlled by H_0. This active feedback is the physical origin of the effective non-Hermitian coefficient introduced in the reduced Hamiltonian description.

3. BOUNDARY VALUE PROBLEMS OF NON-HERMITIAN TOPOLOGICAL BEAM

To capture the nonlocal and actively controlled dynamics, we modify the bending-moment constitutive relation by augmenting the local Euler–Bernoulli term with an active, nonlocal curvature-feedback contribution. In the frequency domain, the bending moment is written as

$$M(x, \Delta x) = -D(x, \Delta x)\, b(x) - P \sum_n \delta(x - x_n(\Delta x))\; b(x + \delta x), \tag{S10}$$

where $b(x) = \partial_x^2 w(x)$ is the curvature associated with the transverse displacement $w(x)$. The local flexural rigidity $D(x, \Delta x)$ is a periodic modulation parametrized by the synthetic shift Δx with period l_a. The second term encodes the programmed nonlocal feedback: a point-like actuator array applies bending moments at the periodic locations

$$x_n(\Delta x) = n l_a - \delta x - \Delta x, \tag{S11}$$

while the injected moment at $x = x_n$ is proportional to the curvature evaluated at the spatially offset sensing point $x_n + \delta x$. The coefficient P is the effective feedback stiffness under the point-source approximation [4]. Using the electromechanical mapping in Eq. (S9), it is given by

$$P = \alpha_c\, H_0, \tag{S12}$$

where α_c collects the piezoelectric constants and patch geometry, and H_0 is the programmable transfer function. Equation (S10) therefore represents a nonlocal and generally nonreciprocal bending law, in which the sensor–actuator offset δx and the synthetic shift Δx together control the active coupling.

With the same harmonic ansatz, the Euler-Bernoulli equation of motion becomes

$$\frac{d^2 M(x)}{dx^2} = -\omega^2\, m(x, \Delta x)\, \hat{w}(x), \tag{S13}$$

where $m(x, \Delta x)$ is the linear density translated by Δx. Substituting Eq. (S10) into Eq. (S13), we have

$$\frac{\partial^2}{\partial x^2}\left[D(x, \Delta x) \frac{\partial^2 w(x)}{\partial x^2} + P \sum_n \delta\left(x - \hat{x}_n\right) \frac{\partial^2 w(x + \delta x)}{\partial x^2} \right] = \omega^2 m(x, \Delta x) w(x). \tag{S14}$$

Here the material distributions $D(x, \Delta x)$ and $m(x, \Delta x)$ are periodic with lattice period l_a in the sense that

$$\begin{aligned} D(x + l_a, \Delta x) &= D(x, \Delta x + l_a) = D(x, \Delta x), \\ m(x + l_a, \Delta x) &= m(x, \Delta x + l_a) = m(x, \Delta x). \end{aligned} \tag{S15}$$

Moreover, Δx parametrizes a rigid translation of the periodic profiles, so one can equivalently write

$$D(x, \Delta x) = D(x - \Delta x), \qquad m(x, \Delta x) = m(x - \Delta x), \tag{S16}$$

where $D(x)$ and $m(x)$ are l_a-periodic functions.

In our study, the metabeam is modeled with free–free boundary conditions, consistent with the experimental configuration in which the beam ends are not clamped or attached to external fixtures. This choice avoids additional constraints from supports and enables a direct comparison between the theoretical model and the laboratory setup. For a free end of an Euler–Bernoulli beam, both the bending moment and the shear force vanish at the two ends,

$$M(x_b) = -D(x)\, \partial_x^2 w(x)\big|_{x=x_b} = 0, \qquad V(x_b) = -\partial_x \left[D(x)\, \partial_x^2 w(x) \right] \big|_{x=x_b} = 0, \qquad x_b \in \{0, L\}. \tag{S17}$$

In our specimen, $D(x)$ is piecewise constant because the thickness is piecewise constant, so $\partial_x D(x) = 0$ almost everywhere (except at internal discontinuities). As a result, the free-end conditions reduce to

$$\partial_x^2 w(x)\big|_{x=x_b} = 0, \qquad \partial_x^3 w(x)\big|_{x=x_b} = 0, \qquad x_b \in \{0, L\}. \tag{S18}$$

Other boundary conditions could be imposed depending on the support configuration (e.g., clamped ends require $w = \partial_x w = 0$, while simply supported ends enforce $w = M = 0$), which would modify the mode spectrum and can suppress or alter boundary-localized states. Here we adopt free boundaries because they most faithfully represent the experimental setup.

Equations (S14) and (S18) together define a closed boundary-value problem for the complex eigenfrequency spectrum and mode shapes. In particular, under open boundaries they determine both the spectrum of skin modes and the boundary-localized TEMs.

4. TWO-BAND REDUCTION AND EFFECTIVE DIRAC BOUNDARY-VALUE PROBLEM

Equation (S14) is a nonlocal differential equation with periodic coefficients. While its Bloch bands can in principle be obtained numerically (e.g., by mode expansion or finite-element eigenfrequency analysis) [5], a full continuum treatment is not ideal for the present purpose: it obscures the band-edge mechanism and does not yield compact, closed-form relations for the TEM eigenfrequency, decay rate, or the delocalization threshold needed for morphing design. In addition, for the non-Hermitian case the open-boundary bulk/skin spectrum is governed by the GBZ in the complex plane, whose smooth parameter tracking is numerically delicate for the full model, making direct non-Bloch invariant evaluations (including the Chern number on GBZ $\times S^1$) impractical. These considerations motivate a reduced description near the Brillouin-zone edge. In this section, we derive a 2×2 effective Dirac Hamiltonian via a NFE reduction and obtain effective free-end boundary conditions by eliminating the evanescent boundary-layer components intrinsic to the fourth-order Euler–Bernoulli operator, thereby forming a closed reduced boundary-value problem.

A. Nearly-free-electron reduction and effective Dirac Hamiltonian.

To set up the NFE reduction, we rewrite the governing equation in a form that separates a uniform reference beam from the periodic modulation and the active nonlocal feedback. We first decompose the flexural rigidity and mass density as

$$D(x - \Delta x) = D_0 + \Delta D(x - \Delta x), \qquad m(x - \Delta x) = m_0 + \Delta m(x - \Delta x), \tag{S19}$$

where D_0 and m_0 are the unit cell averages, and ΔD and Δm are l_a-periodic functions induced by the height modulation. Substituting Eq. (S19) into Eq. (S14) yields the following operator representation,

$$\left[\hat{L}_0 + \hat{L}_1(x - \Delta x) + \hat{L}_2(x - \Delta x, \delta x)\right] |w(x)\rangle = \omega^2 \left[\hat{m}_0 + \hat{m}_1(x - \Delta x)\right] |w(x)\rangle, \tag{S20}$$

in which $\hat{L}_0$ and $\hat{m}_0$ define the baseline uniform-beam problem, while $\hat{L}_1$, $\hat{m}_1$, and $\hat{L}_2$ collect, respectively, the geometric modulation, the associated mass modulation, and the active nonlocal feedback coupling:

$$\begin{aligned}
&\hat{L}_0 = D_0 \frac{\partial^4}{\partial x^4}, \quad \hat{m}_0 = m_0, && \text{baseline uniform beam,} \\
&\hat{L}_1(x - \Delta x) = \frac{\partial^2}{\partial x^2}\left[\Delta D(x - \Delta x)\frac{\partial^2}{\partial x^2}\right], \quad \hat{m}_1 = \Delta m_1(x - \Delta x), && \text{modulation-induced perturbation,} \\
&\hat{L}_2(x - \Delta x, \delta x) = \frac{\partial^2}{\partial x^2}\left[P \sum_n \delta\Big(x - nl_a - \Delta x\Big)\frac{\partial^2}{\partial x^2}\hat{S}(\delta x)\right], && \text{nonlocal feedback coupling.}
\end{aligned} \tag{S21}$$

Here $\hat{S}(\delta x)$ is the shift operator encoding the sensing–actuation offset, defined by

$$\hat{S}(\delta x)\, w(x) = w(x + \delta x). \tag{S22}$$

We now perform a perturbative reduction near the Brillouin-zone boundary. Let the lattice constant be l_a, so the reciprocal lattice vector is $G = 2\pi/l_a$, and denote the zone-edge wavenumber by $\kappa = G/2$. We expand the Bloch wavenumber k about this degenerate point as

$$k = \kappa + q, \qquad |q| \ll \kappa. \tag{S23}$$

The unperturbed degenerate Bloch-wave solutions at the zone boundary are

$$w_1(x) = e^{\mathrm{i}(\kappa+q)x}, \qquad w_2(x) = e^{\mathrm{i}(-\kappa+q)x}. \tag{S24}$$

These two states serve as the basis $|w_{1,2}\rangle$ for a zone-edge degenerate perturbation analysis. We approximate the perturbed state as a linear combination,

$$|w\rangle = \psi_1|w_1\rangle + \psi_2|w_2\rangle, \tag{S25}$$

with complex amplitudes ψ_1 and ψ_2. Substituting this ansatz into the operator equation and projecting onto $\langle w_1|$ and $\langle w_2|$ yields a 2×2 generalized eigenvalue problem for $\psi = [\psi_1,\, \psi_2]^{\mathrm{T}}$,

$$\sum_{j=1}^{2}\langle w_i|\hat{L}_0 + \hat{L}_1 + \hat{L}_2|w_j\rangle\,\psi_j = \omega^2 \sum_{j=1}^{2}\langle w_i|\hat{m}_0 + \hat{m}_1|w_j\rangle\,\psi_j, \qquad i = 1, 2. \tag{S26}$$

Equivalently, in matrix form,

$$\mathbf{K}\,\psi = \omega^2\,\mathbf{M}\,\psi, \qquad K_{ij} = \langle w_i|\hat{L}_0 + \hat{L}_1 + \hat{L}_2|w_j\rangle, \quad M_{ij} = \langle w_i|\hat{m}_0 + \hat{m}_1|w_j\rangle. \tag{S27}$$

To evaluate the perturbative couplings, we expand the stiffness and mass modulations into Fourier series. For an l_a-periodic profile, we write

$$D(x-\Delta x) = \sum_n D_n\, e^{\mathrm{i}nGx}\, e^{-\mathrm{i}n\phi(\Delta x)}, \qquad m(x-\Delta x) = \sum_n m_n\, e^{\mathrm{i}nGx}\, e^{-\mathrm{i}n\phi(\Delta x)}, \tag{S28}$$

where $\phi(\Delta x) = G\Delta x$. The zeroth-order coefficients D_0 and m_0 are the unit cell averages, consistent with Eq. (S19). Within the two-mode reduction near the zone boundary $\kappa = G/2$, only the first harmonics $D_{\pm1}$ and $m_{\pm1}$ couple the degenerate states, so higher-order terms can be neglected.

The resulting nonvanishing matrix elements in the two-mode subspace are

$$\begin{aligned}
&L_{11}^{(0)} = D_0(\kappa+q)^4, \qquad L_{22}^{(0)} = D_0(\kappa-q)^4, \qquad L_{12}^{(0)} = L_{21}^{(0)} = 0,\\
&L_{12}^{(1)} = \beta, \qquad L_{21}^{(1)} = \beta^*, \qquad L_{11}^{(1)} = L_{22}^{(1)} = 0,\\
&L_{11}^{(2)} = -\xi, \qquad L_{22}^{(2)} = -\xi^*, \qquad L_{12}^{(2)} = \xi, \qquad L_{21}^{(2)} = \xi^*,\\
&m_{12}^{(1)} = \gamma, \qquad m_{21}^{(1)} = \gamma^*, \qquad m_{11}^{(1)} = m_{22}^{(1)} = 0,
\end{aligned} \tag{S29}$$

where $L_{ij}^{(k)} = \langle w_i|\hat{L}_k|w_j\rangle$ and $m_{ij}^{(1)} = \langle w_i|\hat{m}_1|w_j\rangle$ for $i,j\in\{1,2\}$. We introduce the shorthand

$$\beta = D_{+1}\left(\frac{\kappa}{2}\right)^4 e^{\mathrm{i}\phi}, \qquad \gamma = m_{+1}e^{\mathrm{i}\phi}, \qquad \xi = P\left(\frac{\kappa}{2}\right)^4 e^{\mathrm{i}G\delta x/2}e^{\mathrm{i}\phi}, \tag{S30}$$

so that the generalized eigenvalue problem can be written compactly as

$$\begin{bmatrix} D_0(\kappa+q)^4+\xi & \beta-\xi \\ \beta^*-\xi^* & D_0(\kappa-q)^4+\xi^* \end{bmatrix}\begin{bmatrix}\psi_1\\ \psi_2\end{bmatrix} = \omega^2(q)\begin{bmatrix} m_0 & \gamma \\ \gamma^* & m_0\end{bmatrix}\begin{bmatrix}\psi_1\\ \psi_2\end{bmatrix}. \tag{S31}$$

Expanding near ω_0, defined by

$$\omega_0^2 = \frac{D_0\kappa^4}{m_0}, \qquad v_F = \frac{2\omega_0\kappa}{m_0}, \tag{S32}$$

and retaining terms to first order in q, β, and γ, the problem reduces to a standard 2×2 eigenvalue problem

$$\begin{bmatrix} v_Fq+\zeta & \eta \\ \eta^* & -v_Fq+\zeta^*\end{bmatrix}\begin{bmatrix}\psi_1\\ \psi_2\end{bmatrix} = \lambda\begin{bmatrix}\psi_1\\ \psi_2\end{bmatrix}, \tag{S33}$$

with effective parameters

$$\lambda = 2\omega_0\delta\omega, \qquad \alpha = \frac{\beta}{m_0} - \frac{\gamma\,\omega_0^2}{m_0}, \qquad \zeta = \frac{\xi}{m_0}, \qquad \eta = \alpha - \zeta. \tag{S34}$$

Equivalently, Eq. (S33) can be rewritten as

$$\mathcal{H}_{\mathrm{eff}}(q)\psi = \lambda\psi, \tag{S35}$$

where, in the Pauli basis, the effective Hamiltonian is written as

$$\mathcal{H}_{\mathrm{eff}}(q) = d_0\mathbf{I} + d_x\sigma_x + d_y\sigma_y + d_z\sigma_z, \tag{S36}$$

with coefficients

$$d_0 = \mathrm{Re}(\zeta), \qquad d_x = \mathrm{Re}(\eta), \qquad d_y = -\,\mathrm{Im}(\eta), \qquad d_z = v_Fq + \mathrm{i}\,\mathrm{Im}(\zeta). \tag{S37}$$

Solving the eigenvalue problem in Eq. (S35) yields the dispersion relation

$$\lambda_\pm(q) = \mathrm{Re}(\zeta) \pm \sqrt{|\eta|^2 + \big(v_Fq + \mathrm{i}\,\mathrm{Im}(\zeta)\big)^2}. \tag{S38}$$

B. Effective boundary conditions under free ends.

We now derive the effective boundary conditions (EBCs) for the reduced two-mode model. The key difference from standard second-order wave equations is that the Euler–Bernoulli beam equation is fourth order in space, so in addition to the two propagating components it also admits evanescent components that become important near boundaries. These evanescent fields do not represent additional bulk degrees of freedom; rather, they appear as boundary-layer corrections required to satisfy the free-end conditions. Our goal is therefore to project out the evanescent contribution and recast the physical boundary conditions into algebraic constraints on the two propagating-mode amplitudes used in the reduced model.

Left boundary: At the left end $x = 0$, the free boundary conditions in Eq. (S18) read

$$\partial_x^2 w(0) = 0, \qquad \partial_x^3 w(0) = 0. \tag{S39}$$

Near the zone-boundary frequency, the unperturbed Euler–Bernoulli operator admits four spatial roots: two propagating roots $\pm\kappa$ and two evanescent roots $\pm\mathrm{i}\kappa$. Accordingly, we expand the displacement field near the left boundary as a superposition of the two counter-propagating components and the left-decaying evanescent component,

$$|w(x)\rangle = \psi_1 \,|w_1(x)\rangle + \psi_2 \,|w_2(x)\rangle + \psi_3 \left|w_{\mathrm{ev}}^{-}(x)\right\rangle, \tag{S40}$$

where $|w_{\mathrm{ev}}^{-}(x)\rangle = e^{-\kappa x}$. For a sufficiently long beam, the evanescent component localized near the opposite end, $|w_{\mathrm{ev}}^{+}(x)\rangle = e^{\kappa(x-L)}$, is exponentially small near $x = 0$ and is neglected.

Applying $\partial_x^2 w(0) = 0$ gives

$$-\kappa^2\psi_1 - \kappa^2\psi_2 + \kappa^2\psi_3 = 0, \tag{S41}$$

and applying $\partial_x^3 w(0) = 0$ gives

$$-\mathrm{i}\kappa^3\psi_1 + \mathrm{i}\kappa^3\psi_2 - \kappa^3\psi_3 = 0. \tag{S42}$$

Dividing out common prefactors yields

$$\psi_3 = \psi_1 + \psi_2, \qquad \psi_3 = -\mathrm{i}\psi_1 + \mathrm{i}\psi_2. \tag{S43}$$

Eliminating ψ_3 then gives the effective left-boundary constraint on the two propagating amplitudes,

$$(1+\mathrm{i})\psi_1 + (1-\mathrm{i})\psi_2 = 0 \qquad \Rightarrow \qquad \psi_1 - \mathrm{i}\psi_2 = 0. \tag{S44}$$

Thus, after eliminating the evanescent boundary-layer component, the left free end reduces to an algebraic phase relation between the two counter-propagating components in the reduced two-mode subspace.

Right boundary: At the right end $x = L$, the free boundary conditions in Eq. (S18) read

$$\partial_x^2 w(L) = 0, \qquad \partial_x^3 w(L) = 0. \tag{S45}$$

Near $x = L$, we expand the displacement as a superposition of the two propagating components and the right-decaying evanescent component,

$$|w(x)\rangle = \psi_1 \,|w_1(x)\rangle + \psi_2 \,|w_2(x)\rangle + \psi_3 \left|w_{\mathrm{ev}}^{+}(x)\right\rangle, \tag{S46}$$

where $|w_{\mathrm{ev}}^{+}(x)\rangle = e^{\kappa(x-L)}$. Applying the free-end conditions at $x = L$ gives

$$-\kappa^2\psi_1 - \kappa^2\psi_2 + \kappa^2\psi_3 = 0, \qquad -\mathrm{i}\kappa^3\psi_1 + \mathrm{i}\kappa^3\psi_2 + \kappa^3\psi_3 = 0. \tag{S47}$$

Dividing out common prefactors yields

$$\psi_3 = \psi_1 + \psi_2, \qquad \psi_3 = \mathrm{i}\psi_1 - \mathrm{i}\psi_2. \tag{S48}$$

Eliminating ψ_3 leads to the effective right-boundary constraint

$$(1-\mathrm{i})\psi_1 + (1+\mathrm{i})\psi_2 = 0 \qquad \Rightarrow \qquad \psi_1 + \mathrm{i}\psi_2 = 0. \tag{S49}$$

Summary: The free-end boundary conditions therefore reduce to the following algebraic constraints on the two propagating amplitudes:

$$\text{Left boundary:} \quad \psi_1 - \mathrm{i}\psi_2 = 0, \qquad \text{Right boundary:} \quad \psi_1 + \mathrm{i}\psi_2 = 0. \tag{S50}$$

These relations encode the net effect of the evanescent boundary-layer components required by the fourth-order beam equation. In the reduced two-mode description, they provide the effective boundary conditions that close the 2×2 Dirac-like eigenproblem under open boundaries.

C. Remarks on the effective Dirac boundary-value problem.

The effective Dirac eigenproblem in Eq. (S35), together with the effective boundary conditions in Eq. (S50), defines a closed boundary-value problem in the reduced description. This effective problem is asymptotically equivalent to the original continuum boundary-value problem given by Eqs. (S14) and (S18) in the regime of interest: it targets eigenmodes in the vicinity of the Brillouin-zone edge frequency ω_0, where the two-mode truncation captures the dominant zone-boundary coupling, and it assumes a sufficiently long beam so that the evanescent component associated with the opposite end is exponentially suppressed in the boundary layer. Under these conditions, the eliminated evanescent fields are fully absorbed into the algebraic constraints in Eq. (S50), leaving a self-contained 2×2 boundary-value formulation for the propagating amplitudes.

In practice, we treat this reduced formulation as an effective model: the coefficients in Eq. (S35) are calibrated by fitting to the complex dispersion and/or the TEM eigenfrequencies in the band-edge neighborhood. This calibration retains the analytical structure of the reduced boundary-value problem—enabling closed-form expressions for the TEM eigenvalues, decay rates, and the morphing threshold—while providing quantitative accuracy over the parameter range considered.

5. UNITARY TRANSFORMATION AND CONNECTION TO THE NON-HERMITIAN RICE–MELE DIRAC FORM

From the NFE reduction, the effective Hamiltonian can be written in the Pauli basis as (Eq. (S36))

$$\mathcal{H}_{\text{eff}}(q) = d_0\,\mathbf{I} + d_x\,\sigma_x + d_y\,\sigma_y + d_z\,\sigma_z, \tag{S51}$$

with coefficients given in Eq. (S37). We now show that, up to a unitary basis rotation, $\mathcal{H}_{\text{eff}}$ is equivalent to the standard Dirac Hamiltonian obtained by linearizing the (discrete) non-Hermitian Rice–Mele model near the Brillouin-zone boundary.

For reference, the Hermitian Rice–Mele model in momentum space reads [6]

$$H_{\text{RM}}(k,t) = \big[u(t) + v(t)\cos k\big]\sigma_x + \big[v(t)\sin k\big]\sigma_y + w(t)\sigma_z, \tag{S52}$$

where $u(t)$ and $v(t)$ are the intracell and intercell hopping amplitudes and $w(t)$ is a staggered onsite potential. A non-Hermitian extension can be introduced by adding an imaginary contribution to the σ_y channel (equivalently, asymmetric intracell hopping), yielding [7, 8]

$$H^{\text{NH}}_{\text{RM}}(k,t) = \big[u(t) + v(t)\cos k\big]\sigma_x + \Big[v(t)\sin k + \mathrm{i}\frac{\gamma(t)}{2}\Big]\sigma_y + w(t)\sigma_z, \tag{S53}$$

where $\gamma(t)$ quantifies the nonreciprocal coupling. Linearizing Eq. (S53) about the zone boundary $k = \kappa + q$ gives a Dirac form,

$$H^{\text{eff}}_{\text{RM}}(q,t) = \tilde{d}_x\,\sigma_x + \tilde{d}_y\,\sigma_y + \tilde{d}_z\,\sigma_z, \tag{S54}$$

with

$$\tilde{d}_x = u(t) - v(t), \quad \tilde{d}_y = -v(t)q + i\frac{\gamma(t)}{2}, \quad \tilde{d}_z = w(t) \tag{S55}$$

in which the three Pauli components encode the dimerization ($\tilde{d}_x$), the nonreciprocal term and Dirac slope ($\tilde{d}_y$), and the staggered potential that breaks chiral symmetry ($\tilde{d}_z$). In particular, $\tilde{d}_z \neq 0$ places the model in class A, whereas the chiral-symmetric limit corresponds to $\tilde{d}_z = 0$.

To make the correspondence explicit for our continuum metabeam, we apply the unitary transformation

$$U = e^{\mathrm{i}\frac{\pi}{4}\sigma_x} = \frac{1}{\sqrt{2}}\big(\mathbf{I} + \mathrm{i}\sigma_x\big), \tag{S56}$$

which satisfies

$$U^\dagger\sigma_z U = \sigma_y, \qquad U^\dagger\sigma_y U = -\sigma_z, \qquad U^\dagger\sigma_x U = \sigma_x. \tag{S57}$$

The Hamiltonian in Eq. (S36) is transformed into

$$\mathcal{H}(q) = U^\dagger\mathcal{H}_{\text{eff}}(q)\,U = d_0\,\mathbf{I} + d_x\,\sigma_x + d_z\,\sigma_y - d_y\,\sigma_z. \tag{S58}$$

Equation (S58) has the same Dirac structure as Eq. (S54): the σ_x term sets the dimerization channel, the σ_y term carries the Dirac slope, and the σ_z term plays the role of a chiral-symmetry-breaking mass (including the non-Hermitian contribution inherited from d_y). The identity term $d_0\mathbf{I}$ produces a uniform spectral shift and does not affect the topology.

In our metabeam, the coefficients in Eq. (S58) have direct physical origins: v_F sets the Dirac velocity at the zone edge, while d_0 and the imaginary part of d_z originate from the nonlocal active feedback, and d_x and d_y encode the combined effects of passive modulation and active nonreciprocal coupling. This unitary equivalence provides a convenient bridge between the continuum reduction and the familiar Rice–Mele Dirac picture used in non-Hermitian lattice topology.

6. DISPERSION RELATION AND TOPOLOGICAL CHERN NUMBER IN NON-HERMITIAN SYSTEM

With the help of synthetic dimension ϕ, it motivates using a 2D Chern number to characterize the topology even when chiral symmetry is broken by non-Hermiticity. The Berry curvature of the lower band takes the form

$$\mathcal{F}_{q\phi} = \partial_q A_\phi - \partial_\phi A_q, \tag{S59}$$

where $A_{q,\phi} = \langle \psi^L | \partial_{q,\phi} \psi^R \rangle$, $\psi^{L,R}$ are left and right eigenvectors of reduced Hamiltonian, leading to a quantized Chern number

$$C = \frac{1}{2\pi} \int_0^{2\pi} d\phi \int_{-\infty}^{\infty} \delta q \mathcal{F}_{q\phi} = \mathrm{sgn}(v_F). \tag{S60}$$

Evaluating the integral yields $C = \mathrm{sgn}\,(v_F)$, confirming that the topological protection of the edge modes persists even when chiral symmetry is broken due to the staggered potential induced by unit cell shift.

7. ASYMPTOTIC ANALYSIS OF THE DIRAC BOUNDARY-VALUE PROBLEM AND THE GENERALIZED BRILLOUIN ZONE

From Eq. (S35), the wavenumber roots q associated with a given λ are

$$q_j = \frac{-\mathrm{i}\,\mathrm{Im}(\zeta) \pm \sqrt{\big(\lambda - \mathrm{Re}(\zeta)\big)^2 - |\eta|^2}}{v_F}, \qquad j = 1, 2. \tag{S61}$$

The corresponding eigenvectors are

$$\psi^j = \begin{bmatrix} 1 \\ r_j \end{bmatrix}, \qquad j = 1, 2, \tag{S62}$$

where the superscript j labels the eigenvector associated with q_j, and $r_j = -\big(v_F q_j + \zeta - \lambda\big)/\eta$. The general solution is a superposition of the two independent exponentials,

$$\psi(x) = A_1\, \psi^1 e^{\mathrm{i}q_1 x} + A_2\, \psi^2 e^{\mathrm{i}q_2 x}, \tag{S63}$$

with superposition coefficients A_1 and A_2.

Meanwhile, the effective boundary conditions in Eq. (S50) read

$$\begin{aligned} \psi_1(0) - \mathrm{i}\psi_2(0) &= 0, \\ \psi_1(L) + \mathrm{i}\psi_2(L) &= 0. \end{aligned} \tag{S64}$$

Substituting the general solution in Eq. (S63) into Eq. (S64) yields a homogeneous linear system for $[A_1, A_2]^{\mathrm{T}}$,

$$\begin{bmatrix} 1 + \mathrm{i}r_1 & 1 + \mathrm{i}r_2 \\ (1 - \mathrm{i}r_1)\, e^{\mathrm{i}q_1 L} & (1 - \mathrm{i}r_2)\, e^{\mathrm{i}q_2 L} \end{bmatrix} \begin{bmatrix} A_1 \\ A_2 \end{bmatrix} = 0. \tag{S65}$$

A nontrivial solution exists if and only if the determinant of the 2×2 coefficient matrix in Eq. (S65) vanishes, which gives the finite-length spectral condition

$$(1 - \mathrm{i}r_1)(1 + \mathrm{i}r_2) e^{\mathrm{i}q_2 L} - (1 - \mathrm{i}r_2)(1 + \mathrm{i}r_1) e^{\mathrm{i}q_1 L} = 0. \tag{S66}$$

Rearranging Eq. (S66) yields the ratio form

$$e^{\mathrm{i}(q_2 - q_1)L} = \frac{(1 - \mathrm{i}r_2)(1 + \mathrm{i}r_1)}{(1 - \mathrm{i}r_1)(1 + \mathrm{i}r_2)}. \tag{S67}$$

Solving Eq. (S67) determines the open-boundary spectrum, including both skin modes and TEMs.

Taking the modulus of Eq. (S67) yields

$$\exp\big[-(\mathrm{Im}\, q_2 - \mathrm{Im}\, q_1)L\big] = \left| \frac{(1 - \mathrm{i}r_2)(1 + \mathrm{i}r_1)}{(1 - \mathrm{i}r_1)(1 + \mathrm{i}r_2)} \right|. \tag{S68}$$

For generic parameters, the right-hand side of Eq. (S68) remains finite (away from isolated points where $1 \pm \mathrm{i}r_j = 0$). Therefore, in the asymptotic limit $L \to \infty$, Eq. (S68) can remain finite only if the two spatial roots share the same decay rate,

$$\mathrm{Im}(q_1) = \mathrm{Im}(q_2), \tag{S69}$$

which is the GBZ condition in the present two-root reduction [9–11].

Together with Eq. (S61), Eq. (S69) requires the square-root term in Eq. (S61) to be real so that the two roots have identical imaginary parts. This yields the GBZ as the horizontal line

$$\mathrm{Im}(q) = -\,\mathrm{Im}(\zeta)/v_F, \qquad \mathrm{Re}(q) \in \mathbb{R}, \tag{S70}$$

in the complex-q plane.

This GBZ fixes the spatial decay rate of the skin modes under OBC. Substituting Eq. (S70) into the dispersion relation in Eq. (S38), the resulting asymptotic OBC spectrum is bounded by

$$\lambda_{\mathrm{OBC}} \le \mathrm{Re}(\zeta) - |\eta| \quad \text{or} \quad \lambda_{\mathrm{OBC}} \ge \mathrm{Re}(\zeta) + |\eta|. \tag{S71}$$

We emphasize that this asymptotic analysis targets the skin-mode continuum in the large-L limit: the GBZ construction captures the spatial decay and spectral bounds of skin modes, but it does not determine the discrete TEM branches, whose eigenvalues and mode shapes will be discussed in the next section. Moreover, using Eq. (S34) one finds that, in the asymptotic limit $L \to \infty$, the skin-mode spectrum under OBC is independent of the phase shift ϕ. Physically, ϕ parametrizes a unit cell reference translation and enters the reduced Hamiltonian only through the off-diagonal phase factors. For the skin-mode continuum, the GBZ construction fixes the imaginary part of q and the spectral bounds depend only on $\mathrm{Re}(\zeta)$ and $|\eta|$, which are invariant under $\eta \to \eta e^{-\mathrm{i}\phi}$. As a result, sweeping ϕ merely reparametrizes the Bloch basis without changing the asymptotic skin-mode spectrum.

8. NON-HERMITIAN TOPOLOGICAL EDGE MODES

Rather than solving the full open-boundary spectral condition in Eq. (S67) to extract the discrete TEMs, we exploit the fact that their properties are controlled by the local termination at a single boundary. We therefore determine the left-localized TEM from a semi-infinite geometry with a left termination, for which the opposite end plays no role. Similarly, the right-localized TEM is obtained from a semi-infinite geometry with a right termination. In this section, we derive the eigenvalues and mode profiles of the left and right TEMs within this semi-infinite formulation.

A. Eigenvalues of topological edge modes

For an edge-localized TEM, the eigenvalue and mode profile are determined by the local termination at a single boundary; for a sufficiently long beam, the opposite end contributes only exponentially small corrections. In a semi-infinite domain, localization requires decay into the bulk, which selects a single admissible spatial root (for $e^{\mathrm{i}qx}$, $\mathrm{Im}(q) > 0$); the growing root is excluded by setting its coefficient to zero. Accordingly, the TEM ansatz takes the form

$$\psi(x) = A_1\, \psi^1 e^{\mathrm{i}q_1 x}, \tag{S72}$$

where q_1 satisfies $\mathrm{Im}(q_1) > 0$ so that the mode decays away from the left boundary.

For a semi-infinite geometry with a free termination at $x = 0$ and $x \to +\infty$ extending into the bulk, only the left-end effective boundary condition in Eq. (S50) is imposed,

$$\psi_1(0) - \mathrm{i}\psi_2(0) = 0. \tag{S73}$$

Using the eigenvector ratio from Eq. (S35), this condition becomes

$$1 + \mathrm{i}\frac{-\mathrm{i}v_F q_1 + \zeta - \lambda_{\mathrm{TEM}}}{\eta} = 0, \tag{S74}$$

which, together with Eq. (S61), yields the left-TEM eigenvalue

$$\lambda^L_{\mathrm{TEM}} = \mathrm{Re}(\zeta) + \mathrm{Im}(\eta). \tag{S75}$$

Similarly, imposing the free termination at the right edge in a semi-infinite geometry gives

$$\lambda^R_{\mathrm{TEM}} = \mathrm{Re}(\zeta) - \mathrm{Im}(\eta). \tag{S76}$$

Finally, comparing $\lambda^{L,R}_{\mathrm{TEM}}$ with the non-Bloch band boundaries $\mathrm{Re}(\zeta) \pm |\eta|$ shows that the TEM eigenvalues lie inside the non-Bloch gap, since $|\,\mathrm{Im}(\eta)| \le |\eta|$.

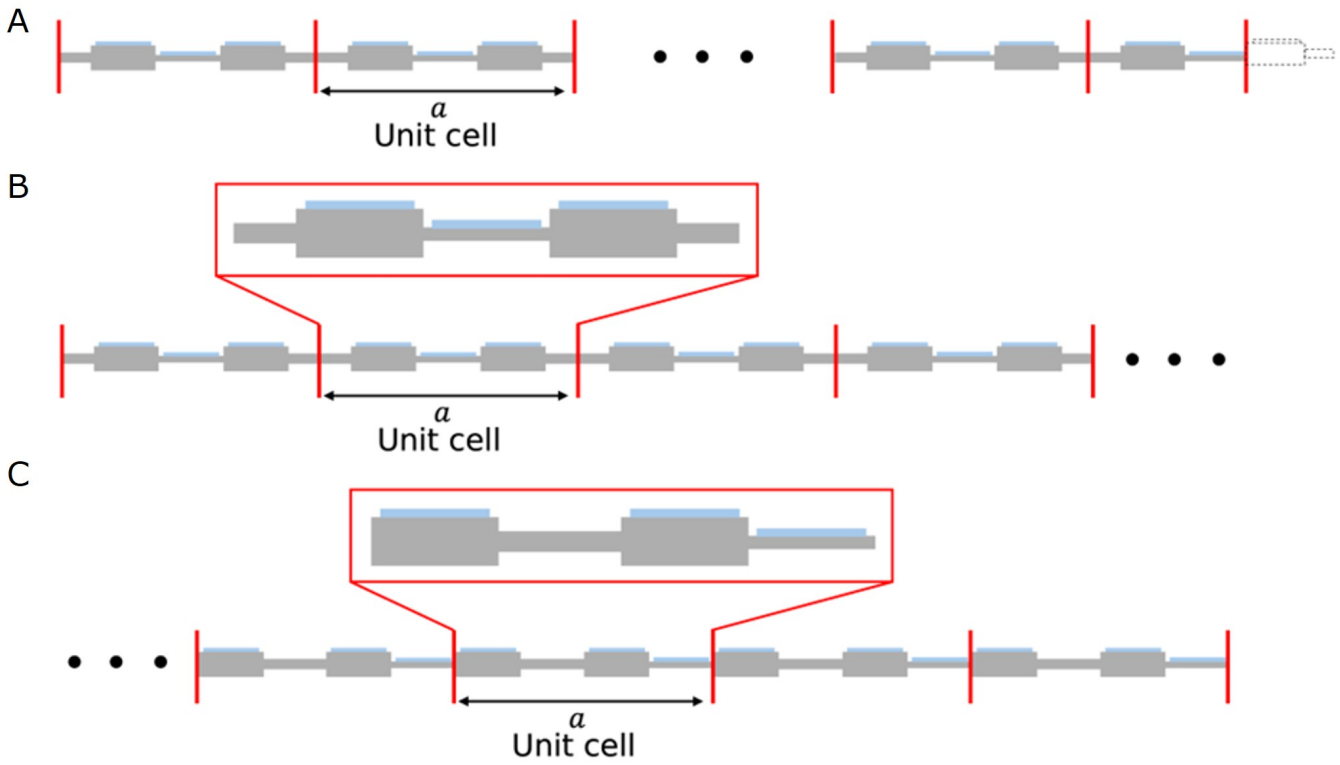

FIG. S2. Schematic showing how boundary termination influences the TEMs of the metabeam. (A) Finite beam used in our study of non-Hermitian morphing, where the dashed portion of the rightmost unit cell is truncated. (B) Semi-infinite metabeam constructed from a unit cell with shift $\delta x = 0$, used to determine the frequency and mode shape of the left edge mode corresponding to the finite beam in (A). (C) Semi-infinite metabeam constructed from a unit cell with shift $\delta x = 0.375 l_a$, used to determine the frequency and mode shape of the right edge mode corresponding to the finite beam in (A).

B. Localization rate of topological edge modes

Substituting the TEM eigenvalues in Eqs. (S75) and (S76) into the wavenumber solution in Eq. (S61) gives the TEM wavenumbers

$$q_{\mathrm{TEM}}^{L,R} = \frac{-\mathrm{i}\,\mathrm{Im}(\zeta) \pm \sqrt{\left(\lambda_{\mathrm{TEM}}^{L,R} - \mathrm{Re}(\zeta)\right)^2 - |\eta|^2}}{v_F}. \tag{S77}$$

The imaginary part of $q_{\mathrm{TEM}}^{L,R}$ defines the localization rate of the TEM,

$$\Gamma_{L,R} = \mathrm{Im}\big(q_{\mathrm{TEM}}^{L,R}\big). \tag{S78}$$

Moreover, in contrast to the skin-mode continuum, the TEM eigenvalues and mode profiles depend explicitly on the phase shift ϕ (equivalently, the unit cell shift Δx). Using Eq. (S34), ϕ enters the reduced Hamiltonian through the complex off-diagonal coupling $\eta(\phi) = \eta_0 e^{-\mathrm{i}\phi}$, which directly affects the boundary-mode condition and the associated spatial root. As a result, sweeping ϕ tunes both the TEM eigenvalue and the decay rate $\mathrm{Im}(q_{\mathrm{TEM}})$, enabling controlled appearance/disappearance and continuous relocalization of the TEM via the synthetic coordinate Δx.

9. NON-HERMITIAN MORPHING OF TOPOLOGICAL MODES

Before analyzing non-Hermitian morphing, we clarify how the boundary termination is treated in a finite metabeam whose length is not an integer multiple of the unit cell period. As sketched in Fig. S3a, the right end is truncated within the last unit cell, so the left and right terminations are inequivalent. For a sufficiently long beam, the two ends are effectively decoupled and the structure can be viewed as the concatenation of two semi-infinite geometries, each characterized by its own local termination. Figures S3b,c illustrate the corresponding constructions: the left termination is represented by a semi-infinite metabeam built from the unit cell reference $\Delta x = 0$, whereas the right termination is represented by a semi-infinite metabeam with a shifted unit cell reference $\Delta x = 0.375\, l_a$.

For skin modes, these two semi-infinite descriptions are related mainly by a reference-point shift, and therefore they share the same asymptotic skin-mode spectrum in the long-beam limit, as discussed at the end of Supplementary Section 7. In contrast, TEMs are termination-sensitive: different local cuts select different edge-mode branches and can move a discrete edge eigenvalue into or out of the spectral gap, as discussed at the end of Supplementary Section 8. This provides a practical way to control the edge-mode content of a finite beam. In the Hermitian limit, we exploit this termination dependence to isolate a single-sided edge mode. As indicated by the open-boundary spectrum in Fig. 2F of the main text, the $\Delta x = 0$ termination places the corresponding TEM near the center of the gap, producing a strongly localized left-edge mode. By contrast, choosing the right termination corresponding to $\Delta x = 0.375\, l_a$ shifts the right-edge branch into the skin-mode spectrum, so that a localized right-edge mode is not supported. This truncation strategy suppresses the hybridization between left and right edge modes in a finite beam and yields a clean, predominantly left-localized TEM as the initial state for the subsequent morphing analysis. Consequently, when discussing the morphing and its localization evolution, it is sufficient to track the left-edge mode selected by the $\Delta x = 0$ termination.

A. Critical delocalization condition for the topological edge mode

Since the termination engineering suppresses the right-edge branch, we focus on the left TEM in the following. The localization of the left TEM is set by the imaginary part of its associated wavenumber. Delocalization occurs when the exponential decay vanishes, i.e., $\Gamma_L = 0$. Using Eqs. (S77) and (S78), this condition is equivalent to

$$\left(\lambda^L_{\mathrm{TEM}} - \mathrm{Re}(\zeta)\right)^2 = |\eta|^2 + \mathrm{Im}(\zeta)^2, \tag{S79}$$

which reduces to the simple threshold

$$\mathrm{Im}(\zeta) = \mathrm{Re}(\eta). \tag{S80}$$

B. Spectral winding transition referenced to the TEM frequency

In non-Hermitian systems, bulk topology can be characterized by how the complex Bloch spectrum winds around a chosen reference frequency in the complex plane. Taking ω_{TEM} as the reference point, we define the spectral winding of the ith band as

$$\mathcal{W}_i = \int_0^{2\pi} \frac{dk}{2\pi} \frac{d}{dk} \arg\left[\omega_i(k) - \omega_{\mathrm{TEM}}\right], \tag{S81}$$

which counts how many times the spectral trajectory $\omega_i(k)$ encircles ω_{TEM} as k traverses the Brillouin zone. The winding can change only when the reference frequency is touched by the bulk spectrum, i.e., when ω_{TEM} coincides with a band boundary. In our two-band model, this transition therefore occurs when

$$\lambda_{\pm}(\pi) = \lambda^L_{\mathrm{TEM}}, \tag{S82}$$

which yields the same threshold as Eq. (S80),

$$\mathrm{Im}(\zeta) = \mathrm{Re}(\eta). \tag{S83}$$

10. BOUNDARY TRUNCATION FOR UNIDIRECTIONAL LOCALIZED TEM

In the metabeam assembled from topologically nontrivial unit cells, the bandgap typically hosts a pair of edge states, localized at two ends of metabeam. These two edge states can hybridize through the finite length, producing the two-end-localized edge modes that are not ideal for cleanly tracking non-Hermitian morphing. To obtain a single, unambiguous localized topological mode, we deliberately engineer the termination by truncating a portion of the rightmost unit cell. This truncating operation suppresses the competing right-localized edge state, while leaving the left-localized edge state intact and strongly localized. The resulting configuration provides a unidirectional edge state for both simulations and experiments, and avoids TEM localization competition when the non-Hermitian control strength is tuned.

11. TRANSFER MATRIX METHOD FOR WAVE DISPERSION WITH PBC AND EIGENFREQUENCY WITH OBC

In this section, we outline the transfer matrix method (TMM) used to derive the dispersion relations of the unit cell and the frequency spectrum of the finite beam for the proposed non-Hermitian topological metabeam. The schematic

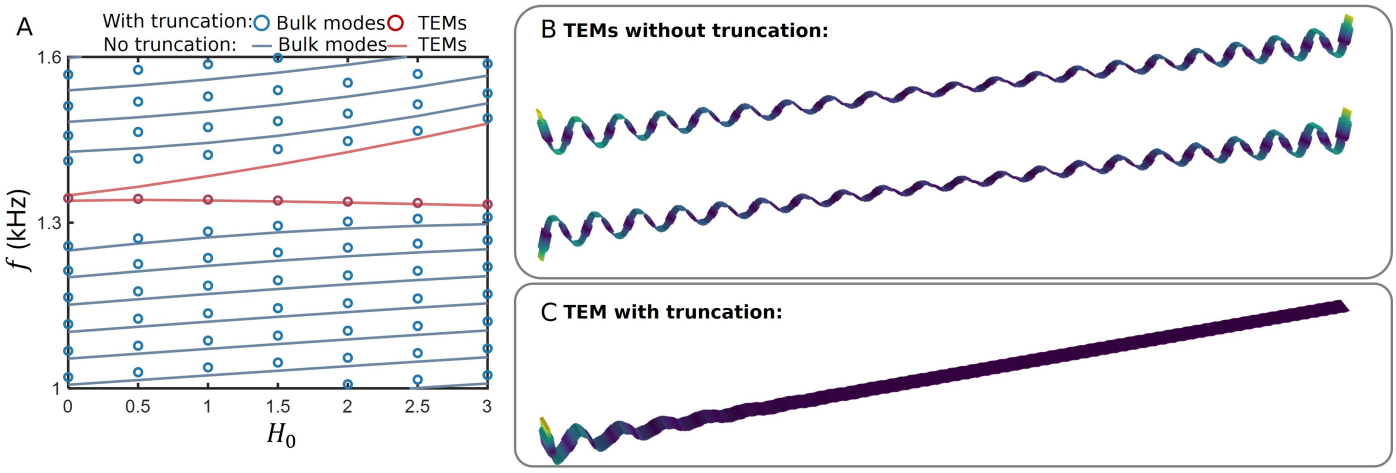

FIG. S3. The effect of truncation on TEMs' frequencies and eigenmode profile. (A) Comparison of frequency spectrum with and without truncation. (B) Eigenmode profile of TEMs without truncation operation. (C) Eigenmode profile of TEM with truncation operation.

representation of the unit cell with PBCs and the 1D non-Hermitian topological metabeam with OBCs is shown in Fig. **??**(a,b). The metabeam's width is chosen as $w_b = 9$ mm, and the total length of unit cell is $l_a = 40$ mm. Three heights are specified as $h_1 = 1.5$ mm, $h_2 = 3$ mm, and $h_3 = 0.85$ mm. We begin by analytically deriving the dispersion relation for the non-Hermitian topological unit cell with non-local active control, using the transfer matrix method [3, 12, 13]. The unit cell is divided into eight sections: Sections 1 and 8 represent the intra-coupling regions, while Sections 4 and 5 serve as the intercoupling regions, each equipped with a piezoelectric sensing patch connected to a charge amplifier. The substrate material is stainless steel, characterized by the following properties: mass density $\rho_s = 7800$ kg/m^3, Young's modulus $E_s = 210$ GPa, and Poisson's ratio $\nu = 0.3$. Each section of the metabeam is modeled under the Timoshenko beam theory, which accounts for both shear deformation and rotary inertia, leading to the governing equations[14]

$$\begin{aligned} m_n \frac{\partial^2 w_n}{\partial t^2} &= \mu_n \left(\frac{\partial^2 w_n}{\partial x^2} - \frac{\partial \phi_n}{\partial x} \right), \\ J_n \frac{\partial^2 \phi_n}{\partial t^2} &= \mu_n \left(\frac{\partial w_n}{\partial x} - \phi_n \right) + D_n \frac{\partial^2 \phi_n}{\partial x^2}, \end{aligned} \tag{S84}$$

where the index n represents the nth section, and $\mu_n = G_n A_n \kappa_n$, $J_n = I_n \rho_n$, $m_n = \rho_n A_n$. The parameters ρ_n, G_n, I_n, κ_n, D_n, A_n, represents the effective mass density, effective shear modulus, effective moment of inertia, effective shear correction factor, effective bending stiffness, and cross-sectional area, respectively. The corresponding bending moment M_n and shear force F_n of nth section can be written as $M_n = -D_n \frac{\partial \phi_n}{\partial x}$ and $V_n = \mu_n(\frac{\partial w_n}{\partial x} - \phi)$. The generalized solutions for w_n and ϕ_n of Eq. (S84) in the frequency domain read

$$\begin{aligned} w_n(x) &= B_n^1 e^{\mathrm{i}k_n^1 x} + B_n^2 e^{\mathrm{i}k_n^2 x} + B_n^3 e^{\mathrm{i}k_n^3 x} + B_n^4 e^{\mathrm{i}k_n^4 x} \\ \phi_n(x) &= C_n^1 e^{\mathrm{i}k_n^1 x} + C_n^2 e^{\mathrm{i}k_n^2 x} + C_n^3 e^{\mathrm{i}k_n^3 x} + C_n^4 e^{\mathrm{i}k_n^4 x}. \end{aligned} \tag{S85}$$

Here, ω is angular frequency, and

$$\begin{aligned} k_n^{1,2} &= \pm \mathrm{i} \sqrt{\frac{-\alpha_n - \sqrt{\alpha_n^2 - 4 D_n \beta_n}}{2 D_n}}, \\ k_n^{3,4} &= \pm \sqrt{\frac{-\alpha_n + \sqrt{\alpha_n^2 - 4 D_n \beta_n}}{2 D_n}}, \end{aligned} \tag{S86}$$

with $\mathrm{i}^2 = -1$, $\alpha_n = m_n \omega^2 D_n / \mu_n + J_n \omega^2$ and $\beta_n = (J_n \omega^2 - \mu_n) m_n \omega^2 / \mu_n$. The relation between the coefficients can be described as

$$\frac{C_n^j}{B_n^j} = \frac{\omega^2 m_n - (k_n^j)^2 \mu_n}{\mathrm{i} \mu_n k_n^j}, \; j = 1, 2, 3, 4. \tag{S87}$$

A state vector field $\mathbf{\Psi}_n(x)$ at nth section is defined as the set of out-of-plane displacement, shear angle, bending moment, and shear force and is expressed as

$$\mathbf{\Psi}_n(x) = \begin{bmatrix} w_n(x) \\ \phi_n(x) \\ M_n(x) \\ V_n(x) \end{bmatrix} = \mathbf{G}_n \begin{bmatrix} B_n^1 e^{\mathrm{i}k_n^1 x} \\ B_n^2 e^{\mathrm{i}k_n^2 x} \\ B_n^3 e^{\mathrm{i}k_n^3 x} \\ B_n^4 e^{\mathrm{i}k_n^4 x} \end{bmatrix} = \mathbf{G}_n \mathbf{F}_n(x) \mathbf{B}_n. \tag{S88}$$

where $\mathbf{B}_n = [B_n^1 \ B_n^2 \ B_n^3 \ B_n^4]^{\mathrm{T}}$. The left and right boundary states of the nth section is expressed as $\mathbf{\Psi}(x_n^-)$ and $\mathbf{\Psi}(x_n^+)$, which are

$$\begin{aligned} \mathbf{\Psi}_n(x_n^+) &= \mathbf{G}_n \mathbf{F}_n(d) \mathbf{B}_n \\ \mathbf{\Psi}_{n+1}(x_{n+1}^-) &= \mathbf{G}_{n+1} \mathbf{B}_{n+1}, \end{aligned} \tag{S89}$$

where d is the length of section. Under the active non-local control, the sensed voltage is amplified and applied to the nearest piezoelectric actuator patch, generating non-local bending moments to achieve non-Hermitian couplings. The relationship of non-local bending moment and the local strain can is expressed as [2, 3]

$$M_{\mathrm{a}} = \alpha \frac{\partial \phi}{\partial x}, \tag{S90}$$

where V_A is the actuating voltage, and α_c denotes the coupling coefficient between the non-local bending strain and the resulting bending moment. Piezoelectric actuator patches are idealized as point sources applied at the center of the patch, generating bending moments [13]. Thus, the piezoelectric actuator patch can be estimated as an effective point-source vector $\mathbf{M}$, which is a function of the non-local state variable. Therefore, the continuity condition at the interface of the nth and $(n+1)$th sections is applied and can be written as

$$\mathbf{\Psi}_n(d) + \delta_{n6} \mathbf{M}_n = \mathbf{\Psi}_{n+1}(0) \tag{S91}$$

where

$$\begin{aligned} \delta_{n6} &= \begin{cases} 0, & n \neq 6 \\ 1, & n = 6 \end{cases}, \\ \mathbf{M}_n &= \mathbf{H} \mathbf{F}_{n-2}(d) \mathbf{B}_{n-2}, \\ H_{ij} &= \begin{cases} \alpha(\omega^2 m_4/\mu_4 - (k_n^j)^2) H_0, & i = 3 \\ 0, & i \neq 3 \end{cases}, \\ i, j &= 1, 2, 3, 4. \end{aligned} \tag{S92}$$

By inserting Eq. (S89) into Eq. (S91), we obtain the iteration relation

$$\mathbf{B}_{n+1} = \mathbf{G}_{n+1}^{-1} \left[\mathbf{G}_n \mathbf{F}_n(d) \mathbf{B}_n + \delta_{n6} \mathbf{H} \mathbf{F}_{n-2}(d) \mathbf{B}_{n-2} \right]. \tag{S93}$$

By recurring Eq. (S93), the state vector at right boundary can be written as

$$\mathbf{\Psi}_8(d) = \mathbf{T}(\omega) \mathbf{B}_1 \tag{S94}$$

where

$$\begin{aligned} \mathbf{T}(\omega) = \mathbf{G}_8 \mathbf{F}_8(d) \Bigg[\prod_{n=2}^{7} \mathbf{G}_n \mathbf{F}_n(d) \mathbf{G}_n^{-1} + \mathbf{H} \mathbf{F}_4(d) \\ \times \prod_{n=2}^{3} \mathbf{G}_n \mathbf{F}_n(d) \mathbf{G}_n^{-1} \Bigg] \mathbf{G}_1 \mathbf{F}_1(d) \mathbf{B}_1 \end{aligned} \tag{S95}$$

By applying the Bloch-Floquet condition $e^{\mathrm{i}kl_a} \mathbf{\Psi}_1(0) = \mathbf{\Psi}_8(d)$ and using Eq. (S89), Eq. (S94) can be written as

$$\left[\mathbf{T}(\omega) - e^{\mathrm{i}kl_a} \mathbf{G}_1 \right] \mathbf{B}_1 = 0. \tag{S96}$$

The the dispersion relations can be obtained by vanishing the determinant of the coefficient matrix of Eq. (S96)

$$\left| \mathbf{T}(\omega) - e^{\mathrm{i}kl_a} \mathbf{G}_1 \right| = 0. \tag{S97}$$

When $\mathbf{H} = 0$, the system reduces to the Hermitian case and the solution of Eq. (S96) gives Hermitian dispersion relations.

Next, we proceed to solve the frequency spectrum of a finite metabeam consisting of M unit cells, where the right half of the last unit cell has been removed, see Fig. **??**(b). For the mth unit cell, the transfer matrix in Eq. (S94) is denoted as $\mathbf{T}^m(\omega)$. The state vector at right boundary of the finite beam can be written as

$$\mathbf{\Psi}(L_a) = \boldsymbol{\mathcal{T}}\mathbf{B}_1, \tag{S98}$$

where

$$\boldsymbol{\mathcal{T}} = \mathbf{G}_4\mathbf{F}_4(d)\left(\prod_{n=2}^{4}\mathbf{G}_n\mathbf{F}_n(d)\mathbf{G}_n^{-1}\right)\left(\prod_{m=1}^{M-1}\mathbf{T}^m\right). \tag{S99}$$

Meanwhile, by using Eq. (S88), the state vector at left boundary of the finite beam can be written as

$$\mathbf{\Psi}(0) = \mathbf{G}_1\mathbf{B}_1. \tag{S100}$$

For the finite 1D topological metabeam, free-free boundary conditions are applied at both ends, requiring the boundary shear forces and bending moments to be zero, leading to

$$\begin{aligned} M(0) &= 0, \quad V(0) = 0 \\ M(L_a) &= 0, \quad V(L_a) = 0 \end{aligned} \tag{S101}$$

Using Eq. (S98) and Eq. (S100), the boundary conditions can be expressed by the coefficient vector $\mathbf{B}_1$, which are

$$\begin{bmatrix} G_{1,31} & G_{1,32} & G_{1,33} & G_{1,34} \\ G_{1,31} & G_{1,32} & G_{1,33} & G_{1,34} \\ \mathcal{T}_{31} & \mathcal{T}_{32} & \mathcal{T}_{33} & \mathcal{T}_{34} \\ \mathcal{T}_{41} & \mathcal{T}_{42} & \mathcal{T}_{43} & \mathcal{T}_{44} \end{bmatrix} \begin{bmatrix} B_{1,1} \\ B_{1,2} \\ B_{1,3} \\ B_{1,4} \end{bmatrix} = 0, \tag{S102}$$

where $B_{1,j}$ is the element of jth row of vector $\mathbf{B}_1$, $G_{1,ij}$ and $\mathcal{T}_{ij}$ are element of ith row and jth column of matrices $\mathbf{G}_1$ and $\boldsymbol{\mathcal{T}}$, respectively. The frequency spectrum of the metabeam with varying cross-sections can be determined by vanishing the determinant

$$\begin{vmatrix} G_{1,31} & G_{1,32} & G_{1,33} & G_{1,34} \\ G_{1,31} & G_{1,32} & G_{1,33} & G_{1,34} \\ \mathcal{T}_{31} & \mathcal{T}_{32} & \mathcal{T}_{33} & \mathcal{T}_{34} \\ \mathcal{T}_{41} & \mathcal{T}_{42} & \mathcal{T}_{43} & \mathcal{T}_{44} \end{vmatrix} = 0 \tag{S103}$$

with the aid of dispersion relations in Eq. (S97). After obtaining the frequency spectra, the coefficient vector $\mathbf{B}_1$ can be obtained by solving the homogeneous equation in Eq. (S102), and the mode shape of finite beam can be obtained by using the transfer matrix.

12. ROBUSTNESS OF NON-HERMITIAN MORPHING OF TOPOLOGICAL EDGE MODES

The non-Hermitian topological morphing of the TEM is robust against disorders. The robustness is demonstrated against intercell coupling (h_1) disorders, as shown in Fig. 12. The localized TEM, delocalized TEM, and re-localized TEM all maintain their modal profiles, indicating the robustness of the morphing process.

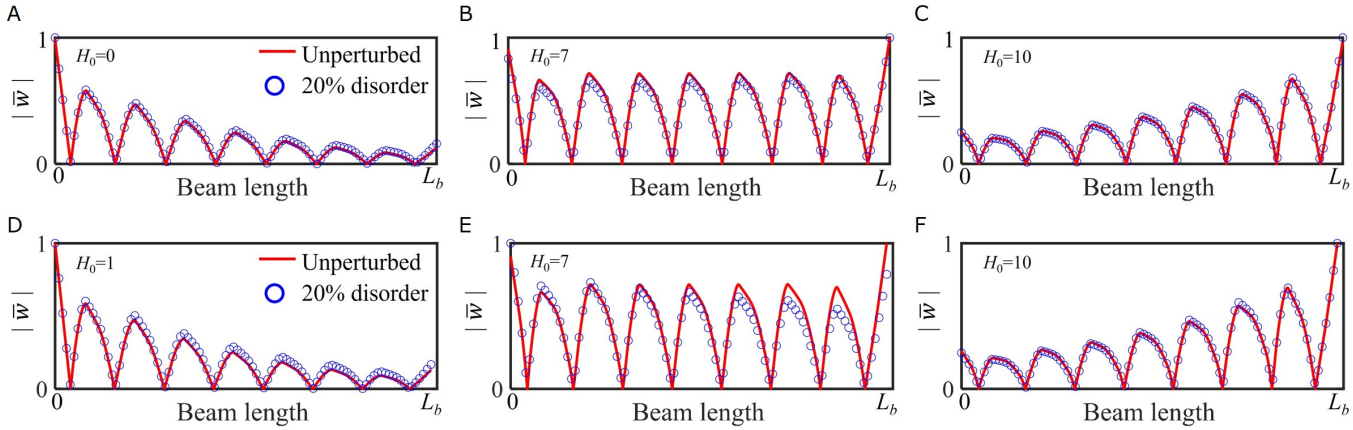

FIG. S4. Robust morphing of the TEM, (A-C) shows the comparison results with and without 20% disorder in intercoupling h_1, (D-F) shows the comparision results with and without 20% disorder in non-Hermitian strength H_0. (A) Localized TEM in the Hermitian case ($H_0 = 0$). (B) Delocalized TEM under critical NHSE ($H_0 = 7$). (C) Re-localized TEM beyond the critical NHSE ($H_0 = 10$). (D) Localized TEM in the weak non-Hermitian case ($H_0 = 1$). (E) Delocalized TEM under critical NHSE ($H_0 = 7$). (F) Re-localized TEM beyond the critical NHSE ($H_0 = 10$). The red lines represent the unperturbed solutions, while the blue dots represent the 10-times averaged results under 20% disorder.

13. EXPERIMENTAL SETUP

Figure S5 shows the experimental setup for measuring the out-of-plane velocity wave field using a 3D SLDV (Polytech PSV-400). Out-of-plane motion in the sample is induced by 20-cycle tone burst signals generated by an arbitrary wave generator (AWG, Tektronix AFG3022C), the centering frequency is set as 1600 Hz. Generated signal is amplified by a power amplifier (PA, Krohn-Hite 7602M), and then applied to the excitation piezoelectric patch. The velocity signals from the SLDV are recorded by the PSV-400 data acquisition system. All instruments are connected to a computer for real-time monitoring, automatic scanning, and signal processing. The substrate beam and meta-plate are fabricated via milling from stainless steel. Piezoelectric patches are affixed to the substrate using conductive epoxy (Circuit Works CW2400). The external circuit, depicted in Fig. S5(c), consists of a charge amplifier, a low-pass filter, and a voltage amplifier. The active circuit is designed by EasyEDA, each PCB consists of four layers to arrange the proposed circuit, which is powered by a DC power source.

14. DESIGN PRINCIPLE OF 2D STACK METAPLATE

Here, we demonstrates the concepts and approximate modeling of the 2D stacking metaplate, which consists of multiple metabeams and weakly coupled by identical struts, as shown in Fig.S1. We roughly see those struts as reciprocal springs which connected the displacement w, the govern equation in can be written as

$$\frac{\partial^2}{\partial^2 x}\left[D(x)\frac{\partial^2 w_n^{(m)}}{\partial x^2}+\sum_N P\delta\left(x-\delta x-Nl_a\right)\frac{\partial^2 w_n^{(m)}(x+\delta x)}{\partial x^2}\right]=-\omega^2\rho A w_n^{(m)}-k_e(w_n^{(m+1)}+w_n^{(m-1)}-2w_n^{(m)}) \quad \text{(S104)}$$

where (m) represents the m^{th} metabeam in metaplate, k_e is the effective flexural coupling between neighbor metabeams, and n is the label of the flexural mode. Due to our focus is on the coupling interaction between multiple individual topological modes, n can be chosen as the specific topological mode, the left side of Eq. S104 can be written as $-\omega_{\text{TEM}}^2\rho A w_{\text{TEM}}^{(m)}(x)$. Thus Eq. S104 can be written as

$$k_e(w_{\text{TEM}}^{(m+1)}+w_{\text{TEM}}^{(m-1)}-2w_{\text{TEM}}^{(m)})=(\omega_{\text{TEM}}^2-\omega^2)\rho A w_{\text{TEM}}^{(m)}(x). \quad \text{(S105)}$$

In our design, metaplate consists of 5 individual beams, corresponds to $m = 1-5$. Eq. S105 can be converted to a 5×5 matrix and eigenvalue problem

$$\begin{bmatrix} k_0'+k_e' & -k_e' & 0 & 0 & 0 \\ -k_e' & k_0'+2k_e' & -k_e' & 0 & 0 \\ 0 & -k_e' & k_0'+2k_e' & -k_e' & 0 \\ 0 & 0 & -k_e' & k_0'+2k_e' & -k_e' \\ 0 & 0 & 0 & -k_e' & k_0'+k_e' \end{bmatrix} w_{\text{TEM}} = -\omega^2 w_{\text{TEM}}, \quad \text{(S106)}$$

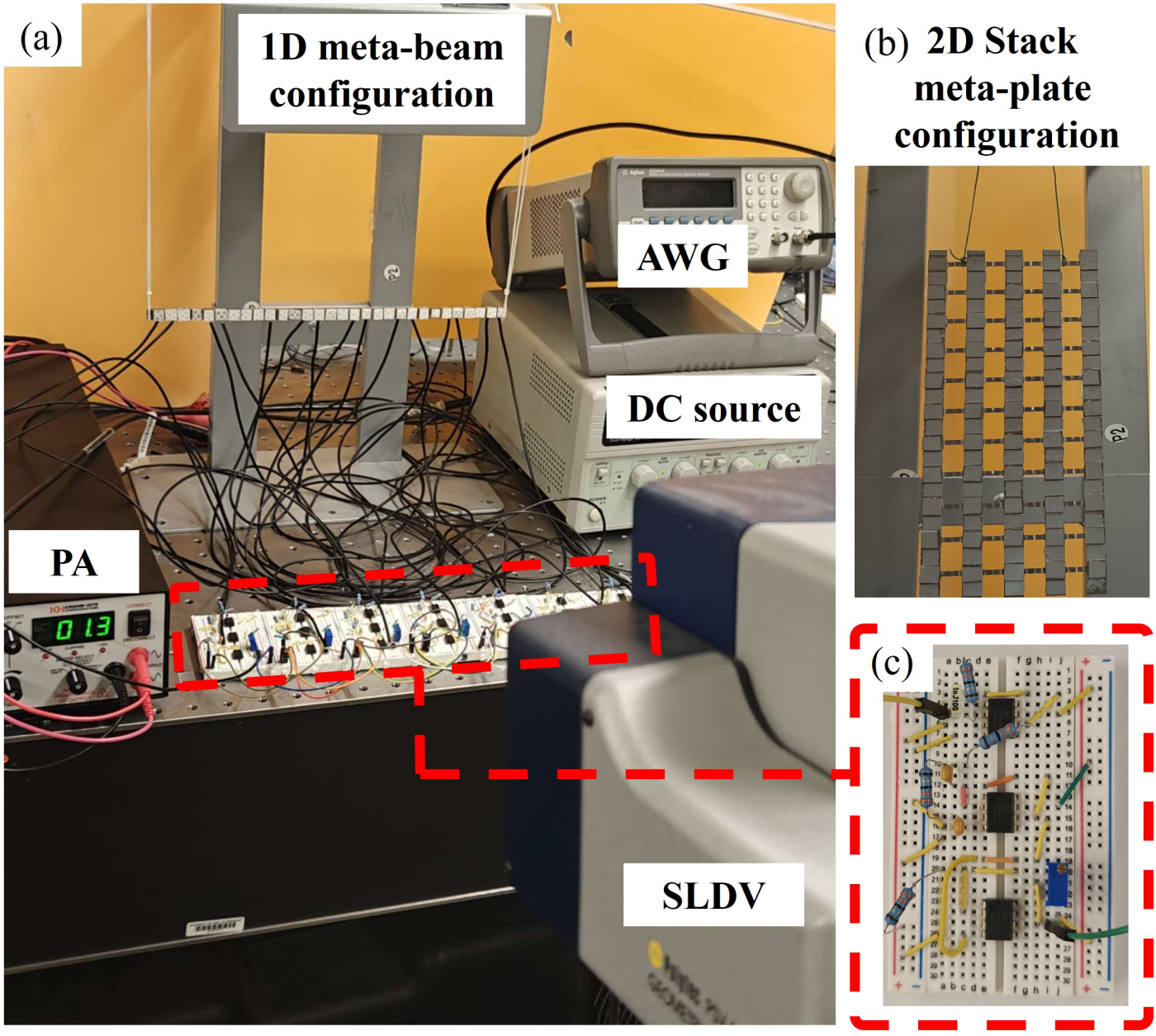

FIG. S5. Experimental setup for (A) the 1D topological metabeam and (B) 2D stacked meta-plate. (C) Magnified view of the non-local control circuit.

where $k_0' = -\omega_{\mathrm{TEM}}^2$, k_e' is the effective coupling coefficient fitted by FEM simulation. We introduce a size coefficient S_c for controlling the strength of coupling between metabeams. The width and height of coupling struts are controlled by S_c, where the new parameters in this case is set as $w_w' = S_c \cdot w_w$, $h_w' = S_c \cdot h_w$. Our experimental demonstration is at $S_c = 1$. This eigenvalue problem in Eq. S106 predicts five eigenmodes with different eigenfrequencies, which evolution to the coupling strength are shown in Fig. S6 A. One eigenfrequency is still ω_{TEM}, corresponds to the eigenvector $\begin{bmatrix}1 & 1 & 1 & 1 & 1\end{bmatrix}^\top$, indicating that all metabeams exhibit the same localized deformation. The remaining eigenvectors and their corresponding topological mode profiles, which show nonuniform deformation across the beams, are also presented in Fig.S6. The reduced-order model accurately predicts the FEM mode profiles. Furthermore, as the effective coupling coefficient k_e' increases, the frequency gaps between the eigenmodes widen. For engineering applications, we select the first TEM for further non-Hermitian morphing and maintain $S_c = 1$ to ensure an appropriate frequency gap between the topological modes, thereby facilitating single-mode operation.

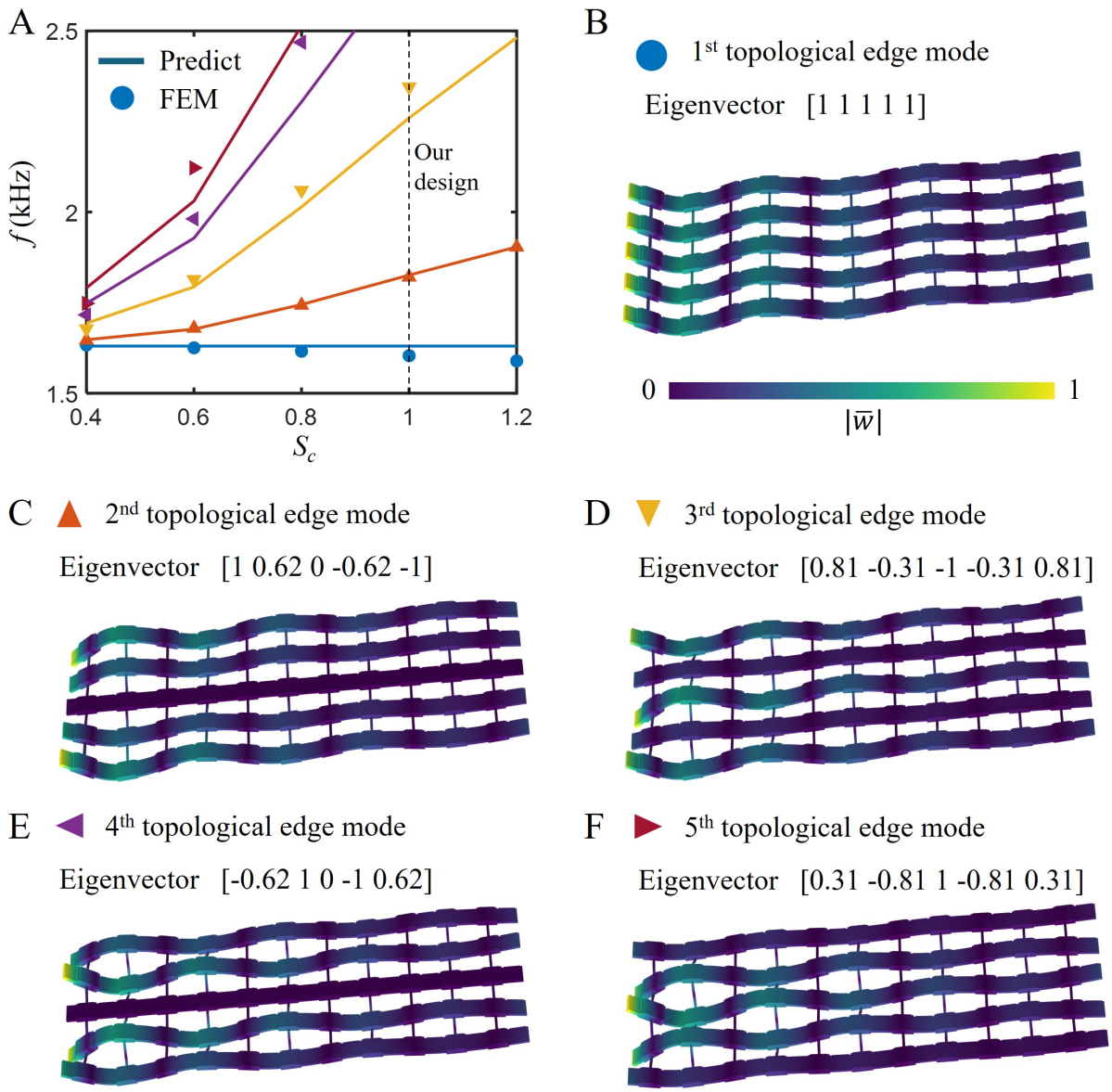

FIG. S6. Frequency spectrum and mode profile of topological mode profiles in 2D stack metaplate. (A) Predicted frequency from reduced model in Eq.S105 and the FEM results. (B) The first topological mode profile in 2D metaplate consists of 5 metabeams when $S_c = 0.4$, the eigenvector from reduced model is $[11111]^\top$. (C) The second topological mode profile from FEM results, the corresponding eigenvector from reduced model is $[1\ 0.62\ 0\ -0.62\ -1]^\top$. (D) The third topological mode profile from FEM results, the corresponding eigenvector from reduced model is $[0.81\ -0.31\ -1\ -0.31\ 0.81]^\top$. (E) The fourth topological mode profile from FEM results, the corresponding eigenvector from reduced model is $[-0.62\ 1\ 0\ -1\ 0.62]^\top$. (F) The fifth topological mode profile from FEM results, the corresponding eigenvector from reduced model is $[0.31\ -0.81\ 1\ -0.81\ 0.31]^\top$.

15. NON-HERMITIAN PHASE TRANSITION AND FREQUENCY SPECTRUM IN 2D METAPLATE

In this section, we discuss the dispersion curves of stack unit cell and non-Hermitian phase transition of TEM in 2D stack meta plate. It's noting that we only consider the first TEM demonstrated at Fig.S6B. The experimental unitcell structure is shown in Fig. S7A. The comparison of the stack unitcell and single unitcell periodic of dispersion curves are shown in Fig. S7B, the effect of struts does not significantly alter the BSBG, as indicating that the topological properties are preserved. Fig. S7C demonstrates the critical non-Hermitian occurs at $H_N = 6$ for stack unitcell, the complex winding passes through the frequency of TEM with OBC. The frequencies of the bulk modes and the TEM of the meta plate and TEM of 1D metabeam are presented in Fig. S7D. It is observed that the frequency of the 2D TEM in the stack metaplate

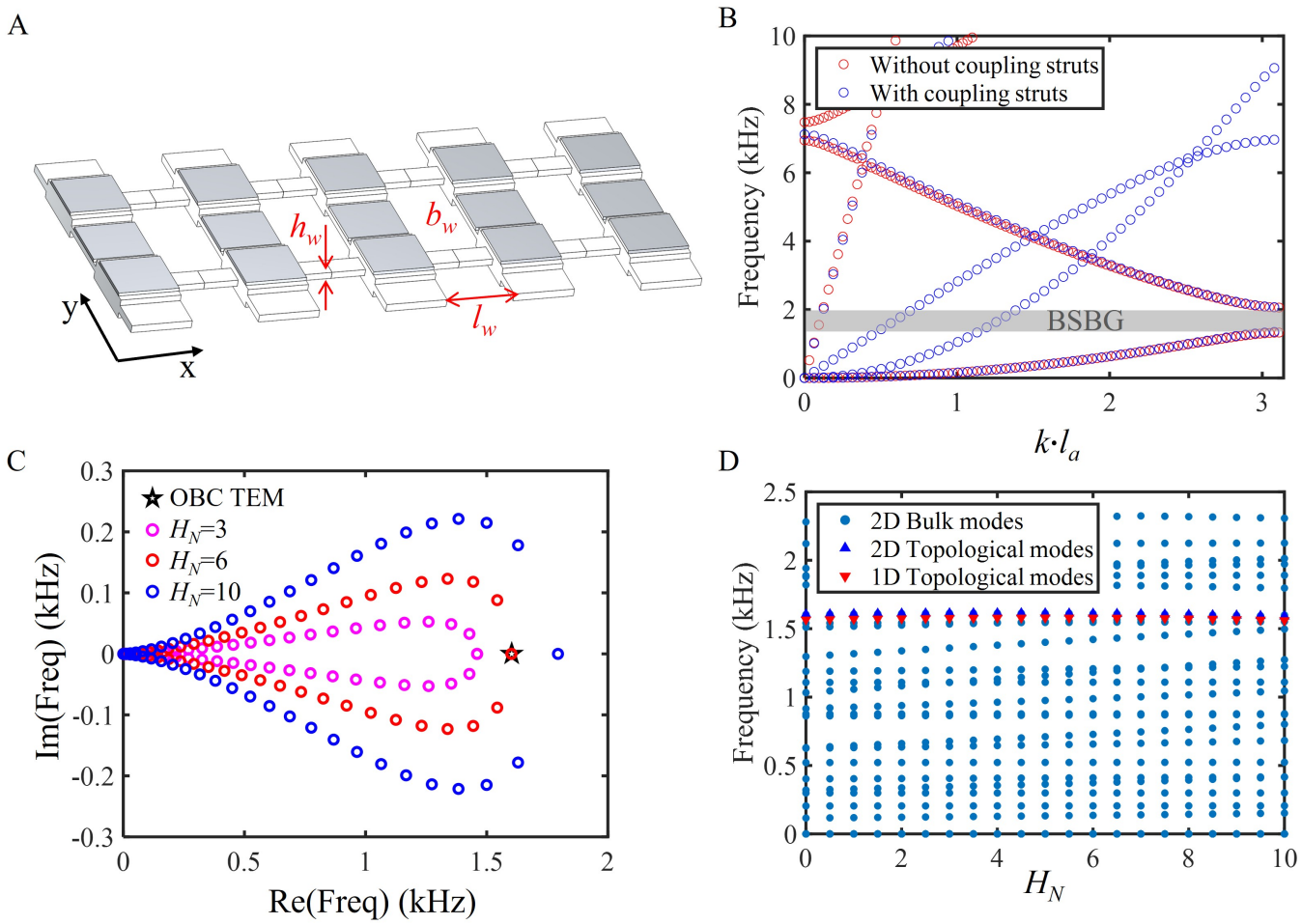

FIG. S7. Reconfigurable topological morphing in the 2D stacked meta-plate. (A) Unit cell structure of the stacked 2D meta-plate. (B) Comparison of dispersion curves for the unit cell with and without coupling struts. (C) Non-Hermitian winding and frequencies of the TEM under OBC for subcritical ($H_N = 3$), critical ($H_N = 6$), and beyond-critical ($H_N = 10$) NHSE conditions. (D) Eigenfrequencies of the TEMs in the 1D topological meta-beam and the 2D stacked meta-plate under varying NHSE strengths.

closely matches that of the 1D topological metabeam across varying strengths of the NHSE. Here, we demonstrate the delocalization and relocalization in 2D metaplate. The Hermitian TEM profile is shown in Fig.S8A, all beams have the same mode pattern localized at the top edge. The delocalization happens with an identical non-Hermitian coupling strength on plate ($H_N = 6$), the NH-TEM shows an extended state (Fig.S8 B). When $H_N > 6$, relocalized NH-TEM is observed (Fig.S8 C), which is localized in the opposite direction (bottom edge).

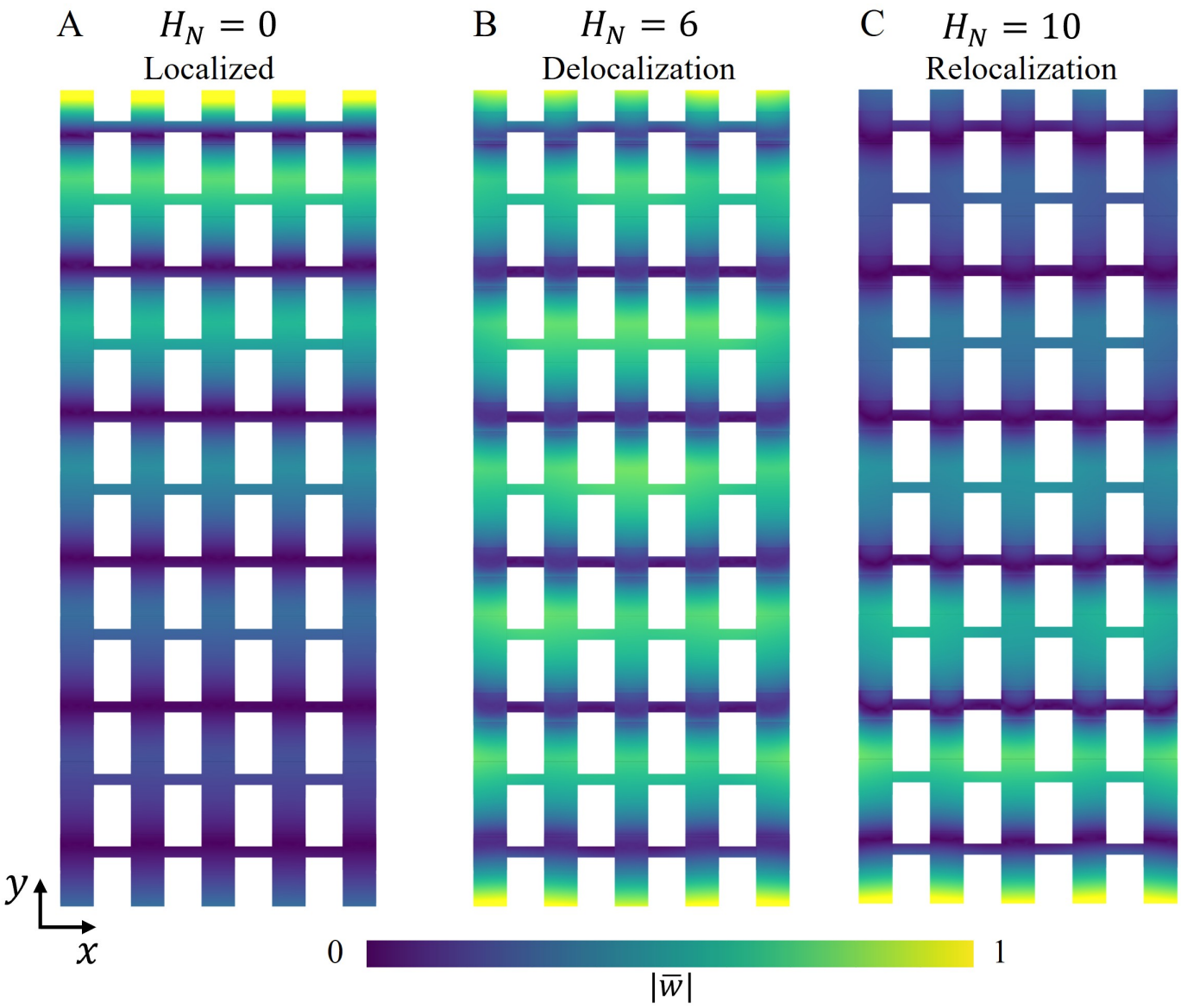

FIG. S8. Reconfigurable topological morphing in the 2D stack metaplate. (A) Simulation results of the passive TEM in he 2D stack metaplate. (B) 2D TEM modal profile exhibiting a delocalized extended pattern with $H_N = 6$. (C) 2D TEM modal profile exhibiting a delocalized extended pattern with $H_N = 10$.

Here, we demonstrate the measured vibration intensity of all scanning points, at the topological frequency (5-th bending mode) and bulk/skin mode frequency (3-th bending mode). The frequency response is first obtained from the vibration signal measured at the upper edge of the middle metabeam. In the passive case, the FFT spectrum exhibits several bending and biaxial-bending resonances, including the fifth bending mode associated with the TEM in the stacked plate, as shown in Fig. S9A. FEM simulations are then used to show the eigenmodes of TEM and the bulk mode (3-rd bending mode), as shown in Fig. S9B and D. The simulated mode shapes agree well with the experimentally measured vibration-intensity profiles along the five coupled metabeams, confirming that the stacked structure preserves both bulk bending modes and the edge-localized TEM inherited from the constituent 1D metabeams.

After activating the active circuits, the resonance spectrum is modified by the imposed non-Hermitian coupling. The active bulk bending modes and TEM exhibits both the non-Hermitian morphing behavior. The measured vibration-intensity profiles follow the FEM predictions, demonstrating that the active control preserves the modal identity of the TEM while reshaping its spatial envelope. These results provide direct experimental evidence that the 2D stacked metaplate supports programmable non-Hermitian morphing of TEM.

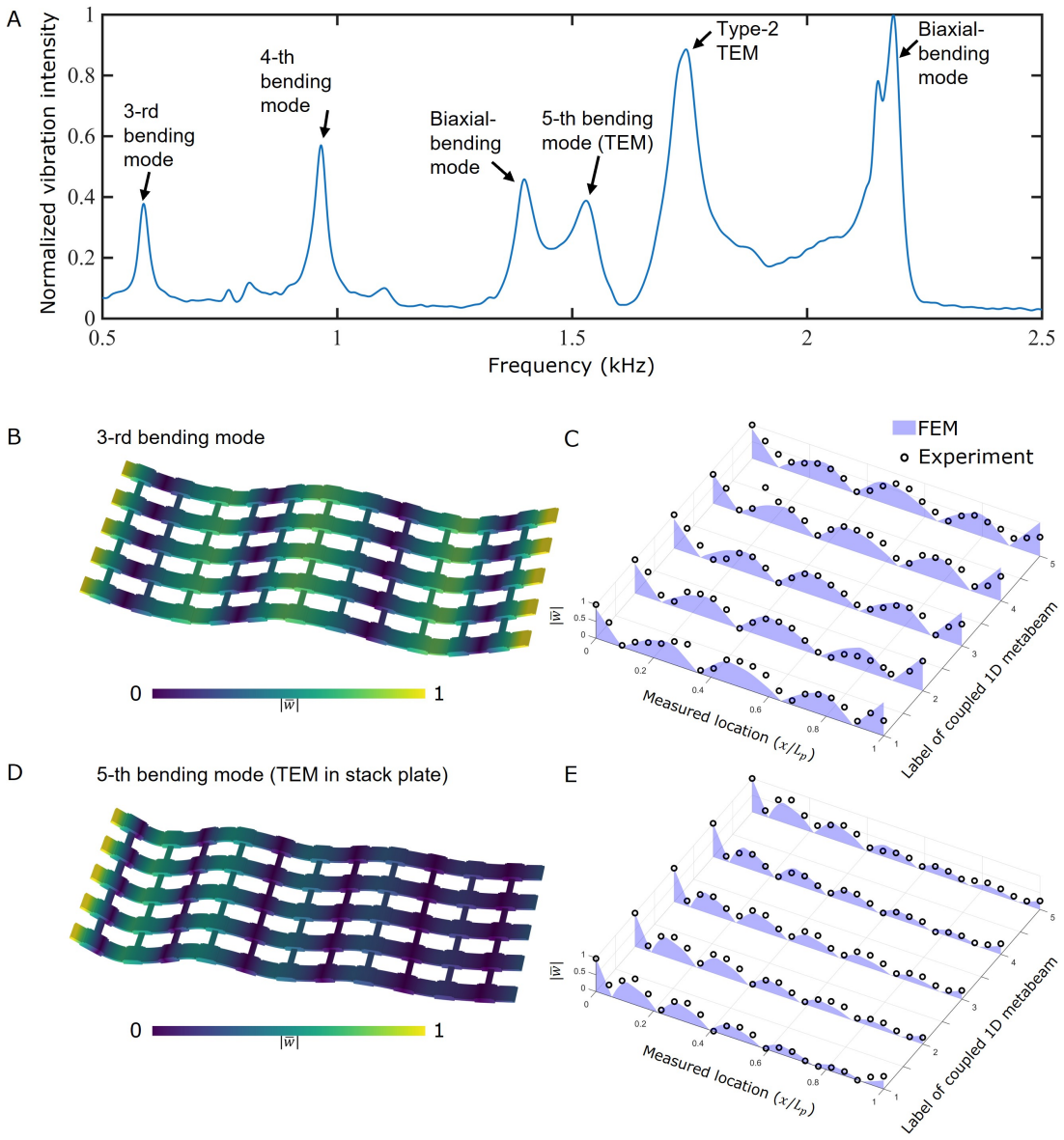

FIG. S9. Passive experimental characterization of the stacked topological metaplate. (A) Measured frequency response of the passive stacked metaplate, obtained from the FFT of the vibration signal recorded at the upper-edge point of the middle metabeam. (B) FEM-simulated mode shape of the third bending mode. The color denotes the normalized out-of-plane displacement magnitude $|\bar{w}|$. (C) Comparison between the FEM-predicted normalized vibration intensity and the experimentally measured intensity for the third bending mode. The purple surfaces denote FEM results, and the black open circles denote experimental measurements. (D) FEM-simulated mode shape of the fifth bending mode, corresponding to the TEM in the stacked plate. (E) Comparison between the FEM prediction and experimental measurement for the TEM vibration-intensity profile.

16. MORE DEFECTS ON SPLITTING PATTERN OF ROBUST TOPOLOGICAL MODE IN METAPLATE

In this section, we examine more defect types on the non-Hermitian topological splitting pattern. In Fig. S11A, two unit cells are converted into Hermitian defects by turning off their active control circuits, so that the local non-Hermitian feedback is removed while the mechanical structure remains unchanged. In Fig. S11B, two void defects are introduced on the two sides of the metaplate by removing the structural material at the labeled locations. In both cases, the topological mode still exhibits a clear energy-splitting pattern, with vibration energy routed toward the two upper corners. These results show that the splitting response is not sensitive to local loss of active control or local structural voids, confirming the robustness of the programmed non-Hermitian topological mode in the metaplate.

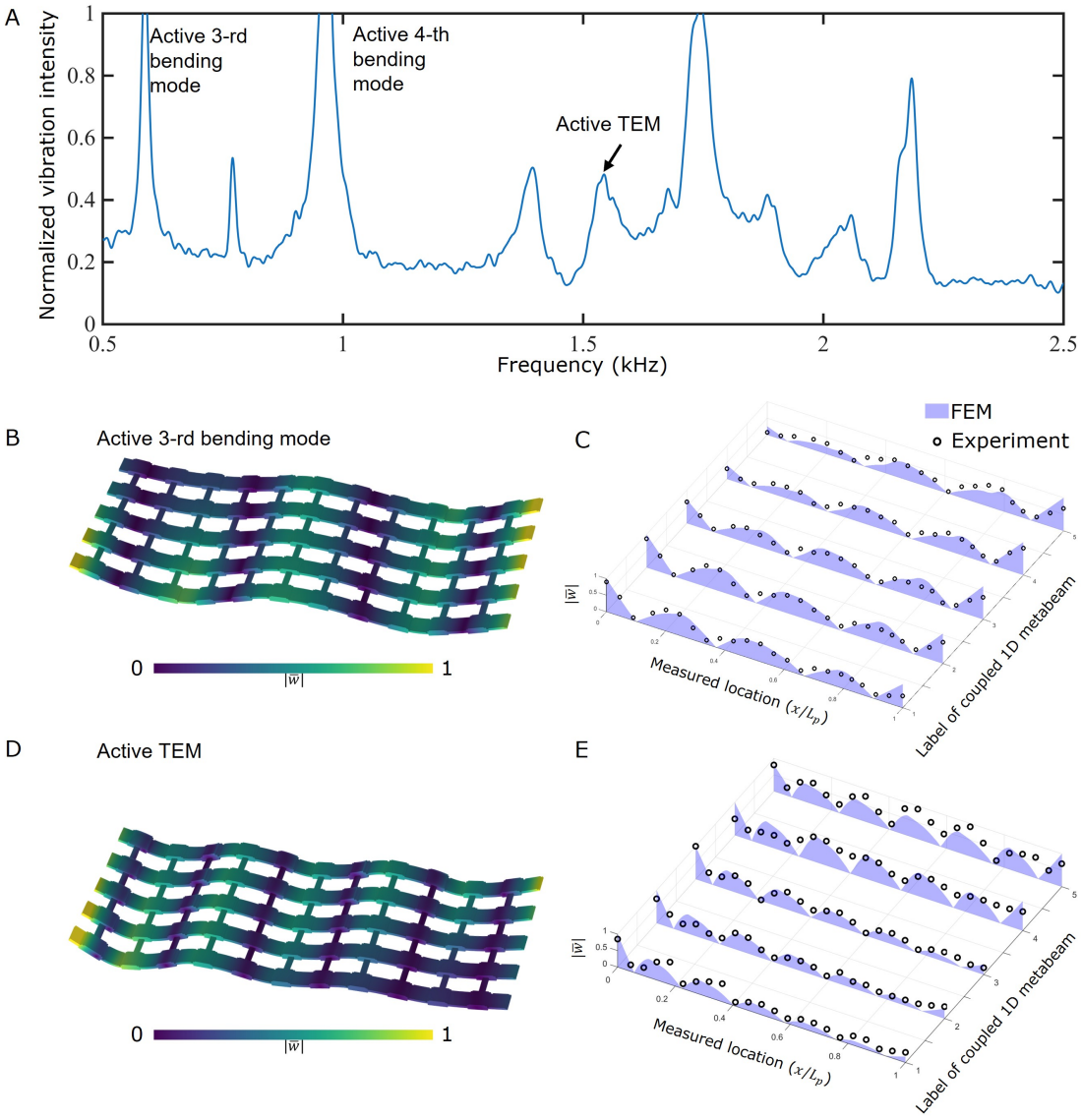

FIG. S10. Active experimental characterization of non-Hermitian morphing in the stacked metaplate. (A) Measured frequency response of the actively controlled stacked metaplate, obtained from the FFT of the vibration signal recorded at the upper-edge point of the middle metabeam. (B) FEM-simulated mode shape of the active third bending mode. The color denotes the normalized out-of-plane displacement magnitude $|\bar{w}|$. (C) Comparison between the FEM-predicted normalized vibration intensity and the experimentally measured intensity for the active third bending mode along the five coupled metabeams. (D) FEM-simulated mode shape of the active TEM under non-Hermitian feedback. (E) Comparison between the FEM prediction and experimental measurement for the active TEM. The measured profile reproduces the simulated non-Hermitian reshaping of the topological mode, validating programmable TEM morphing in the 2D stacked metaplate.

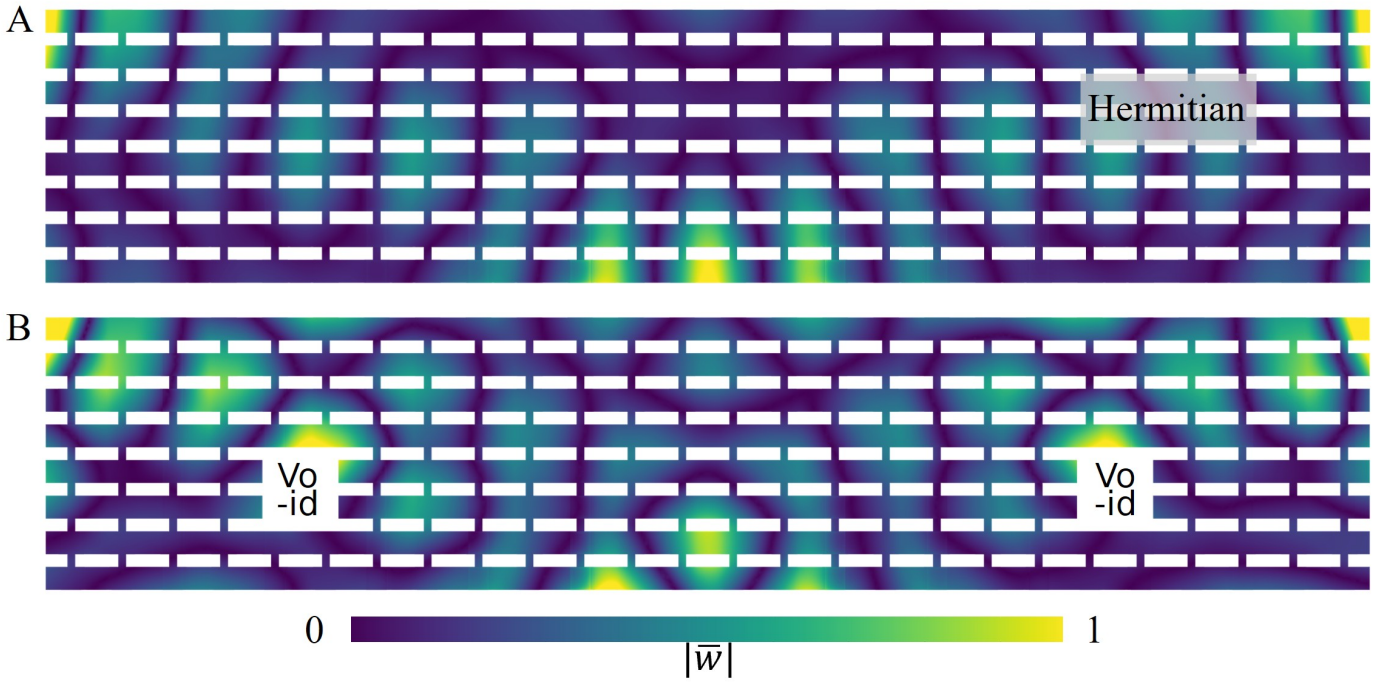

FIG. S11. Demonstration of robust topological mode as energy splitting under two defects. (A) Hermitian defects, the circuits parts are removed in the gray box.(B) Void defects, the structure is removed at the label locations.

Caption for Movie S1. The measured normalized out-of-plane displacement in 1D elastic metabeam, at three representative cases: Localized TEM ($H_0 = 0$), delocalized TEM ($H_0 = 7$), and relocalized TEM ($H_0 = 10$). Movie S1 shows the experimental results of normalized vibration intensity at the TEM resonance frequency.

Caption for Movie S2. The measured normalized out-of-plane displacement in 2D stack metaplate, shows two patterns in Fig. 5: Passive localized TEM (without control), Active localized-to-extended TEM (with control). Movie S2 shows the experimental results of normalized vibration intensity at the TEM resonance frequency of 2D stack plate.

---

[1] Nesbitt W Hagood and Andreas Von Flotow. Damping of structural vibrations with piezoelectric materials and passive electrical networks. *Journal of sound and vibration*, 146(2):243–268, 1991.

[2] Yisheng Zheng, Junxian Zhang, Yegao Qu, and Guang Meng. Adaptive nonreciprocal wave attenuation in linear piezoelectric metastructures shunted with one-way electrical transmission lines. *Journal of Sound and Vibration*, 503:116113, 2021.

[3] Qian Wu, Honghua Qian, Yangyang Chen, and Guoliang Huang. Dynamic phononic crystals with spatially and temporally modulated circuit networks. *Acta Mechanica Sinica*, 39(7):723007, 2023.

[4] Yangyang Chen, Xiaopeng Li, Gengkai Hu, Michael R Haberman, and Guoliang Huang. An active mechanical willis meta-layer with asymmetric polarizabilities. *Nature communications*, 11(1):3681, 2020.

[5] Emanuele Riva, Matheus IN Rosa, and Massimo Ruzzene. Edge states and topological pumping in stiffness-modulated elastic plates. *Physical Review B*, 101(9):094307, 2020.

[6] János K Asbóth, László Oroszlány, and András Pályi. A short course on topological insulators. *Lecture notes in physics*, 919(1), 2016.

[7] Shunyu Yao and Zhong Wang. Edge states and topological invariants of non-hermitian systems. *Physical review letters*, 121(8):086803, 2018.

[8] Zlata Fedorova, Haixin Qiu, Stefan Linden, and Johann Kroha. Observation of topological transport quantization by dissipation in fast thouless pumps. *Nature communications*, 11(1):3758, 2020.

[9] Kazuki Yokomizo and Shuichi Murakami. Non-bloch band theory of non-hermitian systems. *Physical review letters*, 123(6):066404, 2019.

[10] Yu-Min Hu, Yin-Quan Huang, Wen-Tan Xue, and Zhong Wang. Non-bloch band theory for non-hermitian continuum systems. *Physical Review B*, 110(20):205429, 2024.

[11] Shaoyun Wang, Honghua Qian, Jiaji Chen, Nan Shao, Wen Cheng, Heng Jiang, Rui Zhu, and Guoliang Huang. Dynamic willis-framework homogenization for metabeams with active scatterers. *Journal of the Mechanics and Physics of Solids*, page 106548, 2026.

[12] Zhenguo Zhang, Feng Chen, Zhiyi Zhang, and Hongxing Hua. Vibration analysis of non-uniform timoshenko beams coupled with flexible attachments and multiple discontinuities. *International Journal of Mechanical Sciences*, 80:131–143, 2014.

[13] Yangyang Chen, Xiaopeng Li, Colin Scheibner, Vincenzo Vitelli, and Guoliang Huang. Realization of active metamaterials with odd micropolar elasticity. *Nature communications*, 12(1):5935, 2021.

[14] Singiresu S Rao. *Vibration of continuous systems*. John Wiley & Sons, 2019.